Multi-Objective Optimization of Cylindrically Arranged Triply Periodic Minimal Surface (TPMS) Porous Structures for Enhanced Thermal and Hydraulic Performance in Microscale Thermal Management

by

Erfan Ahmadinejad

A Dissertation Submitted to the
Graduate School of Sciences and Engineering
in Partial Fulfillment of the Requirements for
the Degree of

Master of Science

in

Mechanical Engineering

KOÇ ÜNİVERSİTESİ

September 9, 2025

Multi-Objective Optimization of Cylindrically Arranged Triply Periodic Minimal Surface (TPMS) Porous Structures for Enhanced Thermal and Hydraulic Performance in Microscale Thermal Management

Koç University

Graduate School of Sciences and Engineering

This is to certify that I have examined this copy of a master's thesis by

Erfan Ahmadinejad

and have found that it is complete and satisfactory in all respects,

and that any and all revisions required by the final

examining committee have been made.

Committee Members:

____

Assoc. Prof. Savas Tasoglu (Advisor)

____

Prof. Alper Kiraz

____

Assoc. Prof. Sevde Altuntas

Date: September 9, 2025

Dedicated with love to my beloved family — Ahad, Fariba, and Farhan. And to my dearest Sara, my loving girlfriend, whose endless support, joy, and passion have been my greatest strength through all these years. Thank you, Sara, for standing by me in every challenge, for bringing happiness into my days, and for being a source of inspiration and comfort even in the hardest moments.

ABSTRACT

Multi-Objective Optimization of Cylindrically Arranged Triply Periodic Minimal Surface (TPMS) Porous Structures for Enhanced Thermal and Hydraulic Performance in Microscale Thermal Management

Erfan Ahmadinejad
Master of Science in Mechanical Engineering
September 2025

This study presents a multi-objective optimization framework for cylindrically arranged Triply Periodic Minimal Surface (TPMS) porous structures, aimed at enhancing thermal and hydraulic performance in microscale heat sinks for electronic cooling. Integrating conjugate heat transfer simulations in COMSOL Multiphysics with genetic algorithms (GA) and machine learning (ML) surrogates in MATLAB, the approach optimizes seven geometric parameters including cell periodicity, inner radius, and radial/axial level-set gradients across four TPMS types (gyroid, diamond, Neovius, primitive) to maximize volumetric Nusselt number (Nu_v) while minimizing friction factor (f) at a constant Reynolds number of 500 and heat flux of 300 W/cm². Direct GA optimization over 30 generations yielded Pareto fronts dominated by gyroid structures, achieving up to 300% Nu_v improvement with controlled f increases, favoring porosities of 0.50–0.60, inner radii of 0.16–0.18 mm, positive axial gradients (0.3–0.8), and high axial/angular cell counts with minimal radial partitioning. Gaussian Process Regression ML models ($R^2 > 0.85$) trained on GA data enabled an indirect GA method, reducing computation time from 400 to 30 hours while preserving solution quality. Feature ranking identified porosity, TPMS surface area, and periodicity as key drivers. CFD analyses confirmed superior flow uniformity and heat flux distribution in optimal designs, with gyroids excelling at high porosities via enhanced connectivity and diamonds at lower porosities through inward-concentrated convection. The cylindrical arrangement outperformed traditional cuboidal lattices in flow equalization and hotspot reduction which advanced TPMS-based thermal management.

ÖZETÇE

Multi-Objective Optimization of Cylindrically Arranged Triply Periodic Minimal Surface (TPMS) Porous Structures for Enhanced Thermal and Hydraulic Performance in Microscale Thermal Management

Erfan Ahmadinejad
Makine Mühendisliği, Yüksek Lisans
Eylül 2025

Bu çalışma, elektronik soğutma için mikroyapılı ısı alıcılarında ısıl ve hidrolik performansı artırmaya yönelik, silindirik olarak düzenlenmiş Üçlü Periyodik Minimal Yüzey (TPMS) gözenekli yapılar için çok amaçlı bir optimizasyon çerçevesi sunmaktadır. COMSOL Multiphysics'te gerçekleştirilen bağıl ısı transferi (conjugate heat transfer) simülasyonları, MATLAB ortamında genetik algoritmalar (GA) ve makine öğrenimi (ML) yaklaşımlarıyla bütünleştirilmiş; yedi geometrik parametre (hücre periyodiklikleri, iç yarıçap, radyal/eksenel seviye-set gradyanları) dört farklı TPMS tipi (gyroid, diamond, Neovius, primitive) üzerinde optimize edilmiştir. Amaç, Reynolds sayısının 500 ve ısı akısının 300 kW/m² sabit tutulduğu koşullarda hacimsel Nusselt sayısının (Nu_v) maksimize edilmesi ve sürtünme katsayısının (f) minimize edilmesidir. Doğrudan GA optimizasyonu, 30 nesil boyunca elde edilen Pareto ön cephelerinde gyroid yapıların baskın olduğunu göstermiştir; bu yapılar, sürtünme artışları kontrol altında tutulurken %300'e varan Nu_v iyileştirmeleri sağlamıştır. Bu sonuçlar, %50–60 gözeneklilik, 0,16–0,18 mm iç yarıçap, pozitif eksenel gradyanlar (0,3–0,8), yüksek eksenel/açısal hücre sayıları ve minimum radyal bölümlendirmeyi avantajlı kılmıştır. GA verileriyle eğitilen Gaussian Süreç Regresyonu tabanlı ML modelleri ($R^2 > 0,85$), dolaylı GA yöntemine imkân vererek hesaplama süresini 400 saatten 30 saate düşürmüş, çözüm kalitesini ise korumuştur. Özellik önem sıralaması, gözeneklilik, TPMS yüzey alanı ve periyodikliği temel belirleyiciler olarak öne çıkarmıştır. Hesaplamalı akışkanlar dinamiği (CFD) analizleri, optimal tasarımlarda üstün akış düzgünlüğü ve ısı akısı dağılımı doğrulamış; yüksek gözenekliliklerde artırılmış bağlantısallık sayesinde gyroidlerin, düşük gözenekliliklerde ise içe yoğunlaşmış taşınımla diamond yapıların öne çıktığını göstermiştir. Silindirik düzenleme, akış dengelenmesi ve sıcak nokta azaltımında geleneksel kübik kafeslere kıyasla daha başarılı bulunmuş, böylece TPMS tabanlı termal yönetimin ilerletilmesine katkı sağlamıştır.

AKNOWLEDGEMENTS

We acknowledge Tubitak 2232 International Fellowship for Outstanding Researchers Award (118C391), Alexander von Humboldt Research Fellowship for Experienced Researchers, Marie Skłodowska-Curie Individual Fellowship (101003361), and Royal Academy Newton-Katip Çelebi Transforming Systems Through Partnership Award (120N019) for financial support of this research. Opinions, interpretations, conclusions, and recommendations are those of the author and are not necessarily endorsed by the TÜBİTAK. This work was partially supported by Science Academy's Young Scientist Awards Program (BAGEP), Outstanding Young Scientists Awards (GEBİP), and Bilim Kahramanlari Dernegi The Young Scientist Award. This study was conducted using the service and infrastructure of Koç University Translational Medicine Research Center (KUTTAM). The authors have no other relevant affiliations or financial involvement with any organization or entity with a financial interest in or financial conflict with the subject matter or materials discussed in the manuscript apart from those disclosed.

TABLE OF CONTENTS

LIST OF TABLES

LIST OF FIGURES

ABBREVIATIONS

Nu_v	Volumetric Nusselt Number
GA	Genetic Algorithm
ML	Machine Learning
CFD	Computational Fluid Dynamics
TPMS	Triply Periodic Minimal Surface
AM	Additive Manufacturing
DL	Deep Learning
f	Friction Factor
Re	Reynolds Number
FEM	Finite Element Method
GPR	Gaussian Process Regression
NSGA-II	Non-dominated Sorting Genetic Algorithm II
ANN	Artificial Neural Network
PMY	Primitive Minimal Y (a specific TPMS type)
FKS	Fischer-Koch S (a specific TPMS type)
LGBM	Light Gradient Boosting Machine
XGBoost	Extreme Gradient Boosting
SVR	Support Vector Regression
GMDH	Group Method of Data Handling
STL	Stereolithography (file format for 3D Mesh)
STEP	CAD file format
IQR	Interquartile Range
IM-HM	Inlet Manifold - Heat Sink Manifold

Chapter 1:
INTRODUCTION

The rapid miniaturization and increasing power demands of modern electronic devices have intensified the need for advanced thermal management strategies to prevent heat-related declines in reliability, performance, and lifespan [1–3].

At the microscale, cooling technologies such as microchannels and porous structures exhibit significantly enhanced thermal management capabilities often orders of magnitude greater than those observed in macroscale systems. This geometric advantage facilitates superior heat transfer rates, efficient dissipation of high heat fluxes, and improved temperature uniformity, making these solutions indispensable for the thermal regulation of compact electronic devices [4–6].

Among emerging microscale cooling architectures, Triply Periodic Minimal Surface (TPMS) structures have demonstrated exceptional potential for thermal management applications, offering a unique combination of high heat transfer efficiency, enhanced surface area, and intrinsically low pressure drop. Recent numerical and experimental studies confirm that these geometries outperform conventional finned and channel-based designs by enabling superior convective heat transfer and more uniform thermal distribution under both laminar and turbulent flow regimes [7–10].

TPMS structures, especially gyroids, have shown great promise for thermal management applications due to their high surface area and interconnected pathways. Most recent studies have evaluated these structures in regular cuboidal arrays within straight flow channels, rather than complex or application-specific geometries. For instance, introducing gradient wall thicknesses in gyroid units enhanced heat transfer by up to 60.1% and reduced pressure drop by 18.05%, with optimal performance at a 2:4:6 gradient ratio. [7]. Comparative studies across different TPMS types found that PMY performed best at lower volume fractions, while FKS surpassed gyroid at higher porosities due to its balanced flow characteristics [8]. Experimental results also showed that gyroids could improve heat transfer by 55–137% over conventional fins, though slightly less than diamond TPMS due to their open flow paths [9]. Additionally, validated models based on the Darcy–Forchheimer law and Nusselt correlations have been developed to predict pressure drop and heat transfer in these geometries across different flow regimes [10] . Despite these advances, most designs remain limited to simple lattice arrangements, leaving room for innovation in custom-tailored TPMS configurations.

Multi-objective strategies enable explicit balancing of heat transfer gains against pressure drop and structural compliance in TPMS lattices [11–15]. SIMP-based thermal–structural topology optimization produces Pareto fronts whose density fields can be mapped to manufacturable TPMS types, with Primitive showing highest effective conductivity among tested families [11]. Surrogate (Bayesian) optimization rapidly converges strength–permeability (transport-analogue) trade-offs in a few iterations, highlighting efficiency over exhaustive search for coupled geometric parameters [12]. Genetic Algorithms (GAs) decode nonlinear sensitivities of Nu, thermal effectiveness, and pressure drop, confirming inlet velocity as the dominant hydraulic driver and yielding thermal–hydraulic Pareto sets [13]. Field-synergy-guided Gyroid–Diamond hybridization elevates volumetric performance and the composite metric versus single TPMS types, with correlations supplied for reuse [14]. Large GA sweeps report up to 245% volumetric Nusselt improvement with controlled friction factor increases and furnish empirical correlations to navigate convection–resistance trade-offs [15].

A growing body of machine learning (ML) and deep learning (DL) research is augmenting conventional physics- and evolution-based multi-objective heat sink optimization frameworks that previously focused on tripartite trade-offs among heat transfer, pressure drop, and structural compliance in TPMS lattices [11–15]. Recent studies demonstrate that data-driven surrogates can markedly accelerate design-space exploration: (i) DL models with Bayesian-tuned hyperparameters and explainable AI achieve high-fidelity transient prediction for PCM–metal foam composite heat sinks, while clarifying the relative influence of PCM type, fraction, foam material, porosity, and heat flux [16]; (ii) ensemble and kernel methods (LGBM, XGBoost, SVR, ANN) trained on Latin Hypercube - sampled numerical datasets for gradient metal foam heat sinks using micro-encapsulated PCM slurry reveal that Reynolds number and pore density dominate friction factor, while slurry loading and graded porosity significantly elevate Nusselt number (up to 66.96% increase) [17]; (iii) ANN plus greedy search optimization of parallel plate fin heat sinks formalizes alternative, application-aligned objectives, enabling up to 80–85% reduction in ΔP with negligible heat transfer penalty and substantial mass savings (37–68%) compared with baseline high-performance designs [18]; and (iv) hybrid numerical-symbolic modeling using the Group Method of Data

Handling (GMDH) captures multifactor microchannel enhancements (wall slip, porous media, PCM integration, geometry and rheology variations), explaining cumulative thermal performance gains exceeding 80% relative to the base configuration with an interpretable surrogate [19]. Collectively, these advances shift heat sink development toward rapid, data-driven, multi-constraint optimization that complements earlier topology optimization and genetic algorithm approaches. However, a notable research gap remains in ML/DL frameworks have yet to be systematically developed and validated for TPMS-structured heat sinks, particularly for integrating simultaneous thermal-hydraulic objectives.

This study fills a critical research gap by presenting, for the first time, a comprehensive multi-objective optimization framework dedicated to cylindrically arranged TPMS porous structures for microscale heat sink design in electronic cooling. Unlike previous works that have mainly focused on conventional TPMS topologies or limited parametric explorations, this approach integrates conjugate heat transfer analysis in COMSOL Multiphysics with a multi-objective genetic algorithm in MATLAB to simultaneously maximize the Nusselt number and minimize the friction factor. A broad seven-dimensional geometric design space covering cell density, morphology, and spatial gradients is explored, making the optimization both deeper and more generalizable. To further advance the field, machine learning models are incorporated not merely as surrogates for computational efficiency, but also as tools for revealing hidden correlations between structural features and thermal-hydraulic performance. Together, these contributions establish a novel methodology that goes beyond conventional CFD-driven optimization, offering new insights and practical pathways for the design of next-generation TPMS-based heat sinks.

Chapter 2:
METHODS

2.1 Geometry

2.1.1 Heat Sink Design for Thermal Management

As outlined in the Introduction, this work aims to optimize a TPMS structure for enhanced heat transfer. To enable this investigation, a representative heat-sink (computational) domain was defined. The chosen geometry follows widely reported configurations for electronic processor cooling systems [20–25], ensuring comparability with prior literature. A key deviation from earlier studies is the intentional shortening of the domain length to reduce computational time, because the emphasis here is confined to the performance of the TPMS core located centrally within the heat sink. Accordingly, geometric refinements unrelated to the TPMS itself such as alternative outlet arrangements, extended flow development sections, or variations in external dimensions were not pursued. The recent IM–HM heat sink of Xixin Rao et al. [24] (Figure 2.1a) employs a single top inlet and dual side outlets and serves here as a contemporary reference geometry. The modified domain used in this study (Figure 2.1b) replicates that inlet–outlet topology but contracts the planform from 10 mm × 10 mm to 4 mm × 4 mm to reduce computational cost. Inlet size, wall thickness, and internal clearance were preserved so that local hydrodynamic and thermal conditions at the TPMS region remain representative. Side outlets are modeled as simple, unpartitioned openings; no manifolds or diffuser segments were introduced, eliminating ancillary geometric influences. The side view with principal dimensions is shown in Figure 2.1c, and Figure 2.1d illustrates the cylindrically arranged TPMS insert; further specification of the TPMS geometry is provided in Section 2.2.

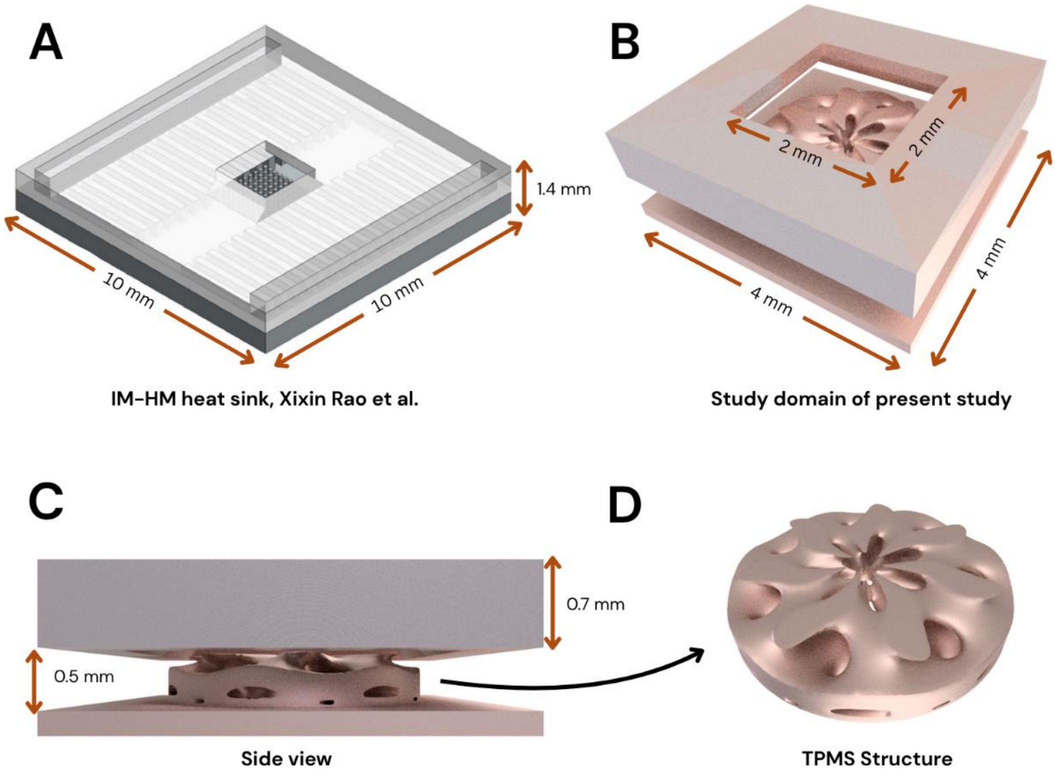

Figure 2.1 Heat Sink Design. (A) Configuration of a well-known heat sink design from literature with its dimensions (reprinted from [24]).(B) Isometric view of the computational domain in the present study, showing overall dimensions and inlet specifications. (C) Side view of the present study domain, illustrating the heights of the TPMS structure and the top part of the heat sink. (D) Example of a cylindrically arranged TPMS structure

2.1.2 TPMS Structure Design

The present study employs a cylindrically arranged TPMS core instead of the conventional rectangular configuration. This choice is motivated by several anticipated advantages, including improved manufacturability, enhanced thermo-hydraulic performance, and greater ease in parametric geometry generation. These benefits are explored in detail in the subsequent sections. The methodology employed to generate the cylindrical TPMS structure is also elaborated upon in this study.

Numerous open-source toolsets for TPMS construction have been documented in the literature [26–29]. Among these, the framework developed by Vafaeefar, Moerman, and Vaughan was selected as the primary resource for this work. This framework offers several distinct advantages, such as its comprehensive coverage of multiple canonical TPMS families, its consistent parameter definitions for tailoring porosity and wall thickness, and its distribution in a format that facilitates seamless integration with the meshing and optimization workflows employed in this study.

TPMS are intricate three-dimensional structures characterized by their zero mean curvature and periodic repetition across all three spatial dimensions. These surfaces are mathematically represented through implicit equations that define a scalar field, where the surface corresponds to the iso-surface at which the scalar field equals zero. The generation of a single TPMS unit cell begins with the selection of a specific surface type, each governed by a unique implicit equation that determines its geometric properties. These equations incorporate trigonometric functions of normalized spatial coordinates, which are scaled to control the periodicity and shape of the surface within a specified domain.

In this study, four distinct TPMS geometries, including Primitive, Diamond, Gyroid, and Neovius, are implemented. Each of these geometries is defined by its implicit equation, which forms the basis for constructing the cylindrical TPMS structures. The mathematical expressions for these geometries, along with corresponding examples, are presented in Table 1. These equations serve as the foundation for the parametric generation of the TPMS configurations utilized in this work. A MATLAB function utilized to generate TPMS structures within a cylindrical domain, incorporating radial and axial level set gradients. The process involves mathematical modeling of TPMS, the creation of a scalar field, and the generation of 3D geometry based on spatial gradients. The function is working within these steps: The cylindrical domain forms the foundational space for TPMS generation. It is defined by radial bounds, angular bounds and axial bounds. The center is specified allowing geometry to be shifted in Cartesian space. Using cylindrical-to-Cartesian transformations, the coordinates are expressed as:

$$X = r \cdot cos(\theta) + cx, \qquad Y = r \cdot sin(\theta) + cy, \qquad Z = z \qquad \text{Eq 2.1}$$

The TPMS scalar field represents the periodic surface mathematically. The periodicity is introduced through normalized arguments u, v, w which scale the radial, angular, and axial coordinates relative to their bounds:

$$u = 2\pi k_r \frac{r - r_{\min}}{r_{\max} - r_{\min}}, \quad v = k_\theta \cdot \theta, \quad w = 2\pi k_z \frac{z - z_{\min}}{z_{\max} - z_{\min}} \qquad \text{Eq 2.2}$$

Here, $kr, k\theta, kz$ control the number of repetitions in each direction. The scalar field $S(u, v, w)$ depends on the chosen TPMS type as illustrated in Figure 2.2.

To customize the geometry of TPMS, spatial gradients are introduced to modify the scalar field both radially and axially. As illustrated in Figure 2.3, the parameters of the cylindrical TPMS are shown, highlighting the radial bounds (R_{min} and R_{max}) which are equal to R_o and r_i in Figure 2.3 and axial bounds (Z_{min} and Z_{max}). The radial gradient adjusts the surface along the radius, introducing a variation that depends on the relative position within the radial bounds. This gradient is influenced by the ratio of level set values at the minimum and maximum radial boundaries, creating a gradual change in the surface properties across the radial direction. Similarly, the axial gradient modifies the surface along the height of the cylinder, ensuring that the geometry adapts based on the axial position. This adjustment is controlled by the ratio of level set values at the minimum and maximum axial boundaries.

Once the scalar field has been modified, the geometry of the TPMS is extracted by identifying the iso-surface at a specified level. This iso-surface represents the final TPMS structure and provides the necessary face connectivity and vertex coordinates for further processing. Caps are added to enclose the structure, ensuring its suitability for manufacturing or simulation purposes. To enhance the quality of the geometry, remeshing is performed, which improves the uniformity of the triangles and edge lengths. This step ensures that the resulting STL files are of high quality and compatible with CFD tools. The finalized TPMS geometry is exported as an STL file for further step.

Design	LevelSet Equation
Primitive	$S = \cos(u) + \cos(v) + \cos(w) = 0$
Diamond	$S = \sin(u) \cdot \sin(v) \cdot \sin(w) + \sin(u) \cdot \cos(v) \cdot \cos(w) + \cos(u) \cdot \sin(v) \cdot \cos(w) + \cos(u) \cdot \cos(v) \cdot \sin(w) = 0$
Gyroid	$S = 3 \cdot (\cos(u) + \cos(v) + \cos(w)) + 4 \cdot \cos(u) \cdot \cos(v) \cdot \cos(w) = 0$
Neovius	$S = \sin(u) \cdot \cos(v) + \sin(v) \cdot \cos(w) + \cos(u) \cdot \sin(w) = 0$

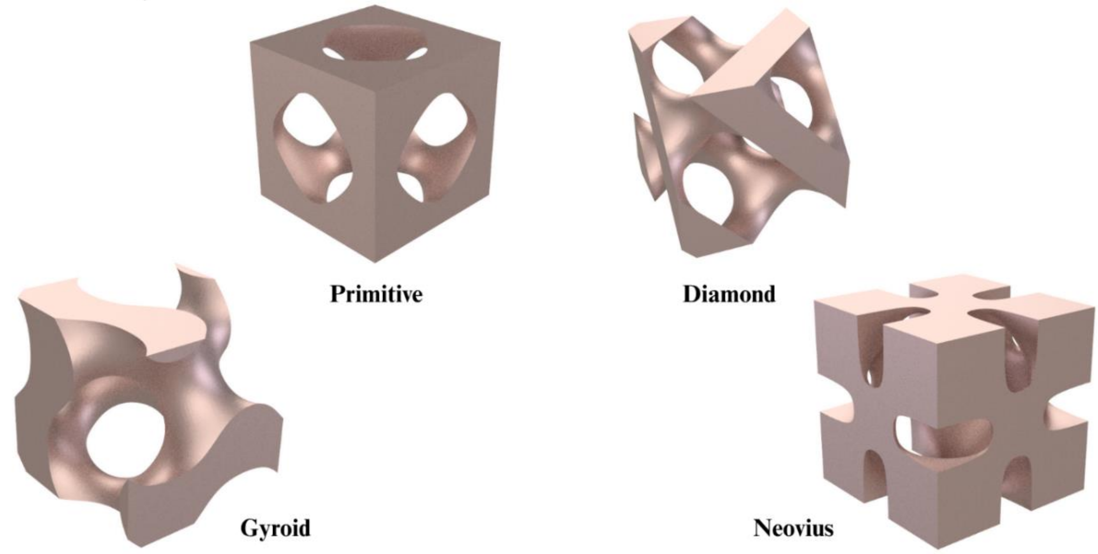

Figure 2.2 Level Set Equations and Single Cell Representations. Table showing the level set equations for each TPMS design type (Primitive, Diamond, Gyroid, Neovius) used in the study, alongside corresponding single cell visualizations of each structure.

2.2 *Parameter Definition*

As explained in the previous section, this study utilizes cylindrical arrangement of TPMS cells. In this section, the geometric parameters used as optimization inputs or as features for machine learning models, which will be discussed in later sections, are presented in Table 2.1 and illustrated in Figure 2.3. There are eight variable parameters in total: seven are numeric values, and one represents the type of TPMS cell.

The TPMS cells are arranged using a cylindrical coordinate system, with variable numbers of repetitions in three directions including axial, radial, and angular ($\mathrm{N}_{\mathrm{axial}}, \mathrm{N}_{\mathrm{radial}}, \mathrm{N}_{\mathrm{ang}}$). The wall thickness of the structure is controlled by the level set value, which was introduced for each geometry type in the previous section. This wall thickness parameter is governed by three distinct variables: the base level set value, which defines the default level set across the entire domain, these two additional level set values create gradients along the axial and radial directions. Importantly, no gradient is introduced in the angular direction to maintain structural symmetry and prevent fluid distribution issues. If all three level set values are equal, the gradient in both axial and radial directions remains zero.

The inner radius is also defined as a variable parameter, as it is expected to influence pressure drop due to its role as the initial region where fluid enters the structure from the inlet. Additionally, certain domain-specific constant parameters are set based on the study domain, which corresponds to the overall dimensions of the heat sink system under investigation.

Table 2.1 Table of TPMS structure variable and Constant Parameters

	Variable	**Variable Description**	**Variable Range**
Variable Parameters	$\boldsymbol{Type}$	$Type\ of\ TPMS\ structure$	G, D, P, N
	$\boldsymbol{N_{ang}}$	$Number\ of\ cells\ in\ angular\ direction$	$[4{,}10]$
	$\boldsymbol{N_{radial}}$	$Number\ of\ cells\ in\ radial\ direction$	$[1, 10]$
	$\boldsymbol{N_{axial}}$	$Number\ of\ cells\ in\ axial\ direction$	$[1{,}5]$
	$\boldsymbol{LS_b}$	$Base\ LevelSet$	$[-0.8, 0.8]$
	$\boldsymbol{LS_{ro}}$	$LevelSet\ at\ r\ =\ ro$	$[-0.8, 0.8]$
	$\boldsymbol{LS_{zo}}$	$LevelSet\ at\ z = 0$	$[-0.8, 0.8]$
	$\boldsymbol{r_i}$	$Inner\ Radius\ of\ the\ cylindrical\ domain$	$[0.05\ mm, 0.2\ mm]$
Constant Parameters	$\boldsymbol{R_o}$	$Outer\ Radius\ of\ the\ cylindrical\ domain$	$1.4\ mm$
	$\boldsymbol{h}$	$Height\ of\ the\ cylindrical\ domain$	$0.5\ mm$
	$\boldsymbol{Mesh}$	$Maximum\ Element\ Size$	$0.05\ mm$

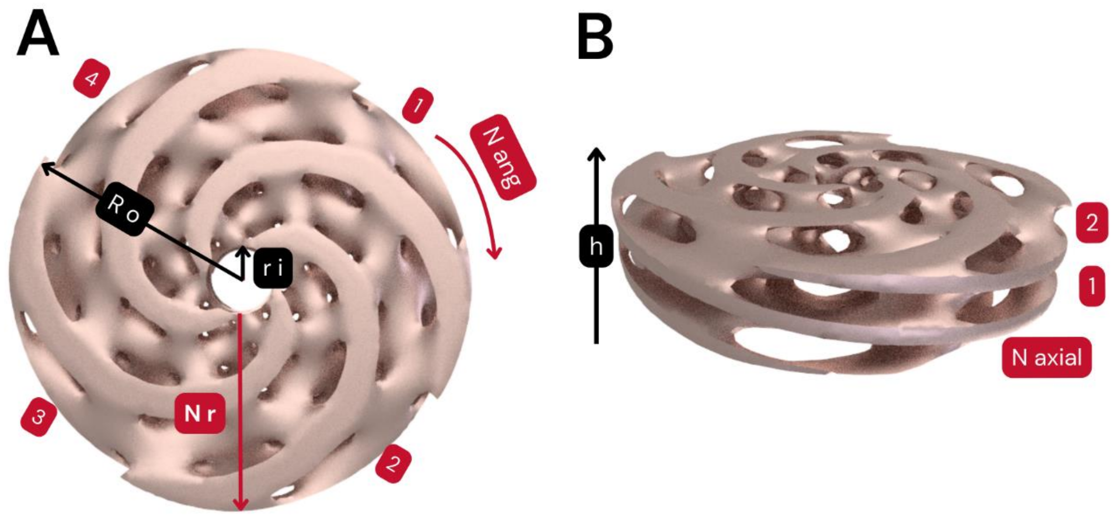

Figure 2.3 Graphical illustration for Geometry Parameters of Cylindrical TPMS structure.

2.3 Computational Fluid Dynamics

The commercial finite element method (FEM) software, COMSOL Multiphysics (v6.3), was utilized to calculate the thermal and fluid performance in this study. The setup of the numerical methods employed is detailed in the following subsections.

2.3.1 Material Properties

In this study, the default material properties for liquid water, as provided by COMSOL Multiphysics, were used to define the coolant. These properties, which are predefined within the software. The specific properties, including density (ρ), viscosity (μ), thermal conductivity (k), and specific heat capacity (C_p), are illustrated in Table 2.2.

Table 2.2 Material Properties of Coolant

Properties	Function	Temperature Range [K]
$\boldsymbol{\mu}$ $[Pa.s]$	$1.3799566804 - 0.021224019151 * T^1 + 1.3604562827E - 4 * T^2 - 4.6454090319E - 7 * T^3 + 8.9042735735E - 10 * T^4 - 9.0790692686E - 13 * T^5 + 3.8457331488E - 16 * T^6$	[273, 413.15]
$\boldsymbol{C_P}$ $[\frac{J}{kg.K}]$	$12010.1471 - 80.4072879 * T^1 + 0.309866854 * T^2 - 5.38186884E - 4 * T^3 + 3.62536437E - 7 * T^4$	[273, 553]
$\boldsymbol{\rho}$ $[\frac{kg}{m^3}]$	$0.000063092789034 * T^3 - 0.060367639882855 * T^2 + 18.9229382407066 * T - 950.704055329848$	[273, 293.15]
	$0.000010335053319 * T^3 - 0.013395065634452 * T^2 + 4.969288832655160 * T + 432.257114008512$	[293.15, 373.15]
$\boldsymbol{k}$ $[\frac{W}{m.K}]$	$-0.869083936 + 0.00894880345 * T^1 - 1.58366345E - 5 * T^2 + 7.97543259E - 9 * T^3$	[273, 553.75]

2.3.2 Geometry & Meshing Sequence

The heat sink design as illustrated earlier in Figure 2.1 features a single inlet with dimensions of 2 × 2 mm and an entry chamfer of 500 µm. In the reference study, they demonstrated that incorporating chamfers at the inlet can reduce pressure drop in microchannels by 63.4% and 72.3%, respectively. This reduction is primarily attributed to the decreased inlet pressure drop, which is often the most significant contributor to pressure losses in such heat sink designs. As mentioned in Section 2.1.1, the overall size of the geometry was shortened in this study to reduce computational time while retaining the essential features of the design. The modified geometry has still one inlet but four outlets in lateral direction.

The CAD model of the top structure was created using the commercial software Fusion 360 (Autodesk Fusion 360, Version 2.0.21550) and saved in STEP format. This file was then imported into the geometry section of COMSOL Multiphysics. The second part of the geometry, consisting of the TPMS structure, was generated using a custom MATLAB (MathWorks Inc., R2023b) function, as detailed in Section 2.1.2, and exported in STL format. When importing the STL file into COMSOL, additional mesh processing steps were necessary to improve the quality of the imported geometry. These steps addressed common defects such as small holes, overlapping mesh elements, small gaps, and unnecessary details. The mesh repair processes in COMSOL included operations such as "Fill Holes" and "Union."

Both parts of the heat sink, the top structure and the TPMS geometry, were imported into COMSOL, and the fluid domain was extracted using the "Create Domain" function. The meshing process was performed using COMSOL's default physics-controlled mesh settings, which utilize free tetrahedral elements. COMSOL automatically adjusts mesh sizes based on the position and size of different geometric components to create an efficient and robust mesh. Additional refinements were applied at corners and boundaries, including boundary layer meshing near walls. This ensures accurate capture of wall shear stress and heat transfer rates, which are critical factors affecting the study's objectives: Volumetric Nusselt Number & Friction Factor.

2.3.3 Physics & Boundary Conditions

Two physics models were used in this study within COMSOL Multiphysics: Laminar Flow and Heat Transfer in Fluids. The assumption of laminar flow is based on the work of Kaixin Yan [30], who investigated the thermo-hydraulic performance of different types of TPMS structures using various turbulence models, such as $k-\omega, k-\epsilon$, Spalart-Allmaras ($S-A$), and laminar flow. Their findings showed that the differences between laminar flow and turbulent models were negligible for both the Nusselt number and friction factor. Therefore, assuming laminar flow is sufficiently accurate for capturing the results in this study. Additionally, laminar flow significantly reduces computational time compared to turbulent models on average 40minutes for laminar flow versus at least two hours for turbulent models. Given the iterative nature of the optimization algorithms used in this study, which involve a massive number of iterations, laminar flow is both computationally efficient and sufficiently accurate.

The study domain features a single vertical inlet and four outlets positioned on the sides, as illustrated with arrows in Figure 2.1.B. The inlet is defined as a velocity inlet, with the velocity calculated using the Equation 2.3:

$$v = \frac{Re.\mu}{\rho.d_h} \qquad \text{Eq 2.3}$$

where μ is the dynamic viscosity of the coolant, ρ is the coolant density, Re is the Reynolds number, and d_h is the hydraulic diameter.

In this study, the Reynolds number is kept constant at a value of 500, which is a reasonable intermediate value based on references [20–25]. The typical Reynolds number range investigated experimentally or numerically in similar heat sink designs is usually between 100 - 1000. The outlets are defined as pressure outlets, set to atmospheric pressure. A no-slip wall condition is assumed for the laminar flow physics, ensuring that the fluid velocity at the walls is zero. The inlet flow temperature is set to 300 K (room temperature). A constant wall heat flux boundary condition is applied to the TPMS structure's surface. This condition reflects real-world scenarios, particularly in electronic processors, where hot surfaces experience constant heat flux. The heat flux value is set to 300 W/cm^2 ,which is based on the literature and represents a high value typically used to investigate heat sink performance under extreme conditions.

2.3.4 Validation of Numerical Method

To ensure the accuracy and reliability of the numerical methods used in this study, a validation process was performed for the laminar flow and heat transfer models. The validation was based on the work of Xixin Rao et al. [24], which investigated an IM-HM heat sink design. This design was selected as a candidate for validating the present numerical method. The geometry of the IM-HM heat sink is illustrated earlier in Figure 2.1.A. It consists of two main parts: top and bottom. The top part includes a single inlet with a chamfer and two parallel side outlets, while the bottom part consists of micro-pillar structures located on top of the hotspot area, which measures $2 \times 2\ mm$ at the center of the hot surface, and rectangular cross-section microchannels extending toward the outlets.

For validation, the geometry and material properties were replicated exactly as described in the reference study. In their work, Xixin Rao et al. solved the numerical problem using Fluent CFD software with the Realizable $k - \epsilon$ turbulence model. However, in the present study, the numerical model was kept in laminar flow mode for two reasons: a) to validate the assumption of laminar flow in the main study case and b) to validate the numerical method itself. Since the reference study was performed using different CFD software, a mesh independence study was conducted to ensure that the chosen mesh accurately captured the results.

The results of the mesh independence study are shown in Figure 2.4.A for both ΔP (average pressure difference between the outlet and inlet) and the maximum temperature of the hot surface of the heat sink design (bottom surface). The number of mesh elements ranged from 100,000 to 13.7 million, and the final mesh size was chosen at 4.8 million elements, as the changes in results beyond this point were very minor, under 1% for both temperature and ΔP. The thermal and hydraulic outputs, specifically the maximum temperature and ΔP, from the reference study and the present numerical method are shown in Figures 2.4.B and 2.4.C. The differences between the outputs for various Reynolds numbers are presented in these plots. The maximum error between the present numerical method and the reference study was 311 Pa for ΔP (≈ 3.9% of the ΔP), which is negligible compared to the overall ΔP values, and $3.17°C$ for maximum temperature (≈ 1.0% of the temperature), which is acceptable within the assumption of laminar flow.

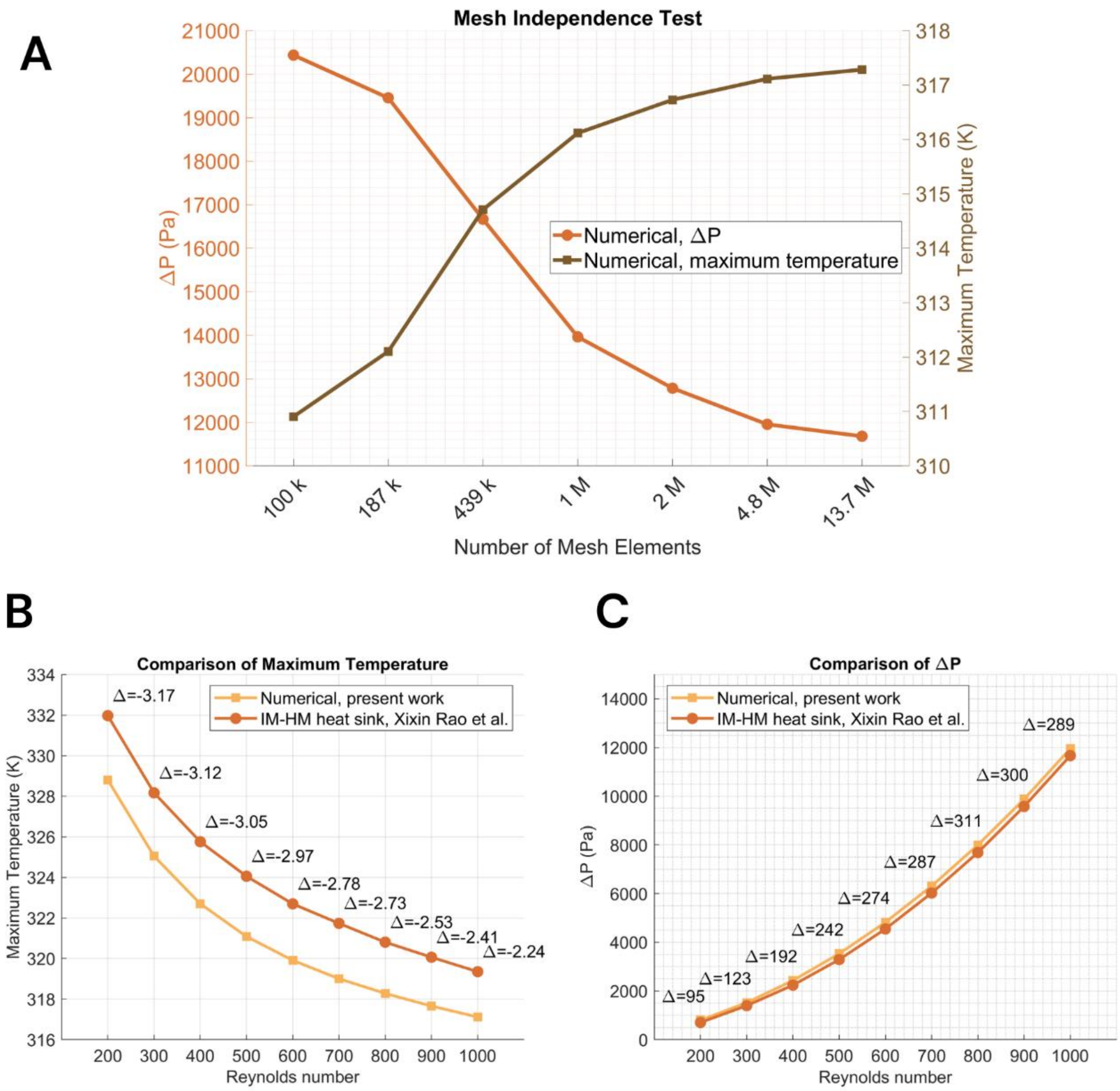

Figure 2.4 Validation of CFD Method. (A) Mesh independence study for the validation analysis. (B) Comparison of maximum temperature between the present numerical method and the reference. (C) Comparison of pressure difference between outlets and inlet for both methods.

2.4 *Key Performance Metrics and Formulations*

In this section, the key performance metrics derived from Computational Fluid Dynamics (CFD) simulations are defined and formulated.

2.4.1 Geometrical Intermediate Outputs

The cylindrical arranged TPMS structures in this study are generated using a MATLAB function, which outputs the geometry as STL files based on the parameters defined in Table 2.1. These parameters allow for significant flexibility in controlling the geometry, including varying the number of cells in three directions, adjusting the inner radius, and applying different level set values to create gradients in two directions. This high degree of controllability provides benefits, such as enabling the creation of diverse individual structures, but it also presents challenges. Specifically, it becomes difficult to theoretically measure key geometrical properties, such as porosity, hydraulic diameter, and surface area of the structure, either through analytical equations (e.g., porosity being a function of level set values with linear relationships for single TPMS cells [29]) or within the MATLAB function itself, as this would require extensive coding and be time-consuming.

These intermediate geometrical outputs, while not direct inputs or objectives, are considered critical because they are frequently reported in literature to influence thermal and flow performance [15,31–33]. To overcome the challenges of measuring these properties theoretically, the calculations are performed numerically after importing the TPMS structures into COMSOL Multiphysics. This approach ensures accurate determination of porosity, hydraulic diameter, and surface area, which are essential for understanding the relationship between geometry and Hydro-Thermal performance. The equations for calculating these intermediate outputs are presented below:

$$\phi = \frac{Vf}{Vt} = \frac{Vf}{Vs + Vt} \qquad \text{Eq 2.4}$$

$$d_h = 4 \times \frac{Vf}{As} \qquad \text{Eq 2.5}$$

where Vf represents the volume of the fluid region within the porous structure (TPMS structure), and Vt is the total volume of the cylindrical region, which includes both the solid (Vs) and fluid regions. The hydraulic diameter (d_h) of the TPMS structure is calculated where As denotes the surface area of the TPMS structure. These metrics are critical for evaluating the geometrical properties of the TPMS structures and their influence on thermal and hydraulic performance.

2.4.2 Hydraulic Performance Metrics

One of the critical aspects of heat sink design and performance is the pressure drop across the system, as it directly impacts the required pumping power and overall energy consumption. To evaluate the flow resistance in porous media, the friction factor (f) is a widely used non-dimensional parameter, extensively studied in previous research [34–37]. In this study, the friction factor is calculated using the following equation:

$$f = \frac{2 \times d_h}{\rho . u_{in}^2} . \frac{\Delta p}{L} \qquad \text{Eq 2.6}$$

In the equation, d_h represents the hydraulic diameter of the porous structure, while is Δp the pressure drops across the structure (Outlet Pressure – Inlet Pressure). The term L denotes the length of the flow of the stream from inlet to outlet. The inlet velocity (u_{in}) calculated using the following equation:

$$u_{in} = \frac{Re . \mu}{\rho . d_h} \qquad \text{Eq 2.7}$$

In the equation, Re represents the Reynold number, and μ is Dynamic viscosity of Water.

2.4.3 Thermal Performance Metrics

To investigate the thermal performance of the TPMS design, this study primarily focuses on evaluating its convective heat transfer characteristics. The Nusselt number (Nu) is a widely recognized parameter for assessing convective performance. However, for pore-scale structures, such as those examined in this study, the volumetric Nusselt number (Nu_v) has been identified as a reliable and well-established metric in the literature [15,38–40]. The volumetric Nusselt number is calculated using the following equations:

$$Nu_v = \frac{h_v . d_h^2}{k} \qquad \text{Eq 2.8}$$

where d_h is the hydraulic diameter of the porous structure and k is the thermal conductivity of the fluid. The volumetric heat transfer coefficient is calculated using the relationship:

$$h_v = h \frac{A_s}{Vf} \qquad \text{Eq 2.9}$$

Furthermore, the heat transfer coefficient is determined as:

$$h = \frac{q^{\cdot}}{\Delta T_{wv}} \qquad \text{Eq 2.10}$$

where $q^{\cdot}$ represents the constant heat flux applied to the TPMS wall, and ΔT_{wv} is the temperature difference between the wall surface and the fluid volume average.

2.5 Machine Learning in Design of TPMS structures

Recent advancements in AI models, particularly ML and DL, have proven effective in solving complex engineering problems, such as prediction and optimization. In this study, due to the intricate TPMS geometry and numerous input parameters, manually identifying relationships between inputs and thermal-hydraulic performance is impractical. AI models are utilized to streamline this process, uncovering correlations and facilitating optimization.

2.5.1 Generation of Dataset

Since the iteration time for each step, including TPMS structure generation, meshing, and CFD analysis to calculate intermediate parameters and performance metrics ranges between 30 and 50 minutes, generating a separate dataset would be highly time-consuming. Instead, the data generated during the genetic algorithm process (Will be explained in section 2.6) was saved for each generation and used as the dataset for training the predictive model. The total number of data points used for each geometry varied due to the genetic algorithm favoring certain types and generating more efficient designs. Specifically, the dataset sizes for gyroid, diamond, Neveius, and primitive structures were 544, 241, 94, and 320, respectively.

2.5.2 Preprocessing

The dataset recorded from the Genetic Algorithm potentially contains many outliers, which may either represent solutions in the Pareto front or dominated points. These outliers arise because evolutionary search explores a wide solution space, where some candidates achieve extreme performance trade-offs while others are far from optimal. Filtering outliers is essential for training the predictive model to ensure robust and reliable results. The method of Interquartile Range (IQR) was applied to filter outliers, using the range defined by Equation 2.11 here.

$$[Q1 - 1.5 \times IQR, Q3 + 1.5 \times IQR] \qquad \text{Eq 2.11}$$

Outliers falling outside this range were removed from the dataset. After removing the outliers, the distribution of the data for the gyroid type, as shown in Figure 2.5. The distribution of the friction factor (f) exhibits a right-skewed shape, indicating a non-normal distribution, with most values concentrated in the lower range. In contrast, the distribution of the volumetric Nusselt number (Nu_v) appears approximately normal, with a symmetric peak near the center and tapering off on both sides. For porosity, the distribution shows a sharp peak around 0.5, with values tapering off on both sides, suggesting a non-normal distribution.

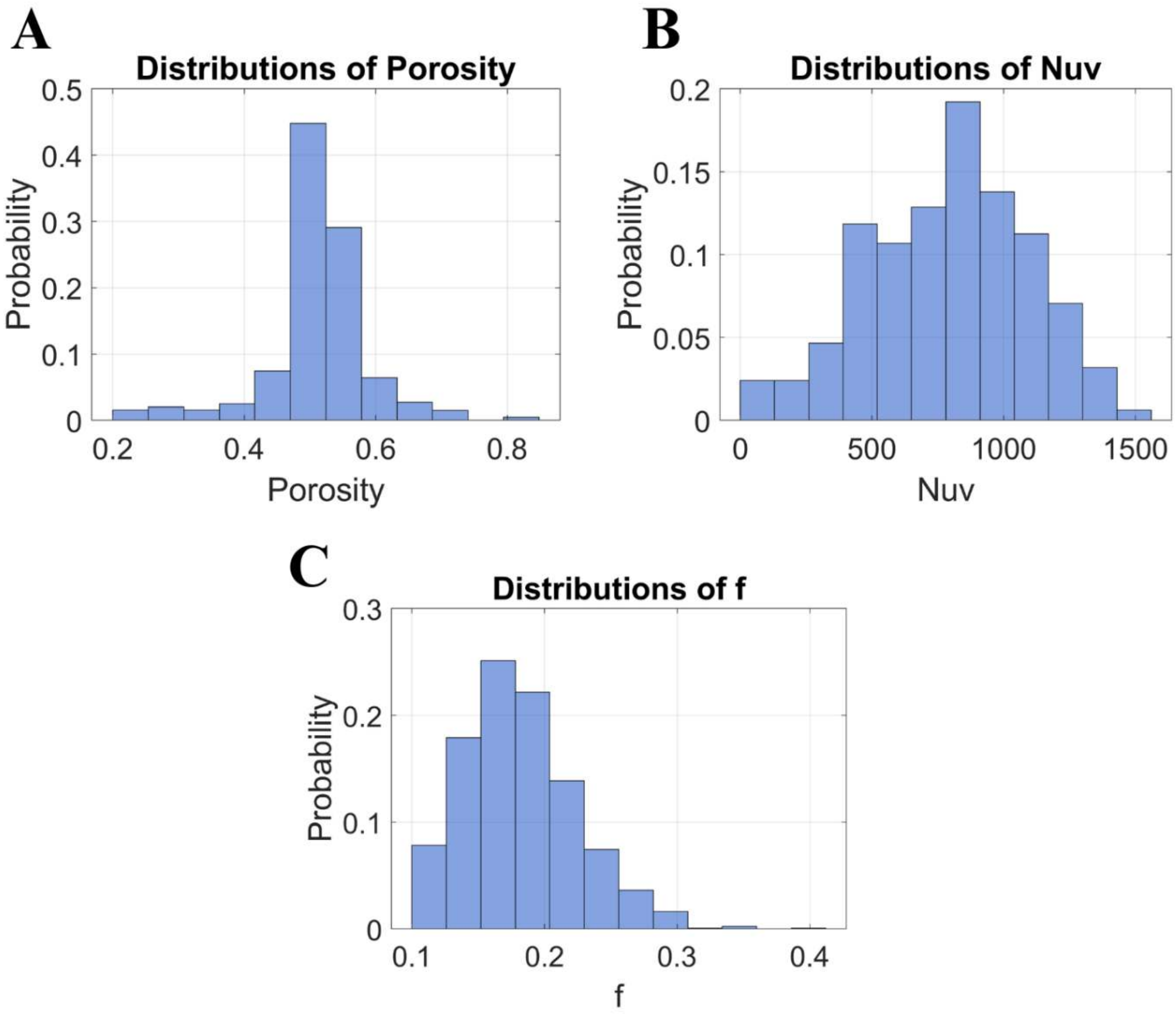

Figure 2.5 Distribution Plots for Gyroid Geometry. (A) Distribution of porosity. (B) Distribution of Nusselt number (Nu_v). (C) Distribution of friction factor (f).

2.5.3 Machine Learning Features

The geometrical inputs, along with intermediate parameters calculated after meshing the geometry, were utilized to derive additional features. This process resulted in the creation of new features, increasing the total number of potential features to 25. The complete list of these features is presented in Table 2.3. The table includes geometrical inputs that are directly used to generate the TPMS structure, intermediate results calculated numerically after the meshing process, and features derived by taking the mean level set values along three directions. Additionally, it incorporates features calculated as differences, ratios, and gradients of the level set values, as well as interactions between porosity, TPMS surface area, and other derived parameters.

Table 2.3 Features Used for Machine Learning Training, Including Geometry Inputs, Evaluated Intermediate Parameters, and Engineered Features.

	Feature	Description	
1	N_{ang}	Number of cells in the angular direction.	Geometry Inputs
2	N_r	Number of cells in the radial direction.	
3	N_{ax}	Number of cells in the axial direction.	
4	baseLevelset	Base level set value used for geometry generation.	
5	levelset_ro	Level set value at the outer radius (r=ro).	
6	levelset_zd	Level set value at the axial position (z=0).	
7	ri	Inner radius of the cylindrical domain.	
8	TPMSAs	Total surface area of TPMS	Intermediate Parameters
9	Porosity	Fraction of void space within the geometry	
10	Vs	Solid volume of the geometry.	
11	Vt	Total volume of the geometry.	
12	Vf	Real fluid volume within the porous structure	
13	dh	Hydraulic diameter of the structure	
14	MeanLevelsetZ	Mean level set value in the axial direction (z)	Engineered Features
15	MeanLevelsetR	Mean level set value in the radial direction (r).	
16	MeanLevelsetTotal	Overall mean level set value across all directions.	
17	Delta_ro	Difference between level set at r=ro and the base level set.	
18	Delta_zd	Difference between level set at z=0 and the base level set.	
19	Ratio_ro	Ratio of level set at r=ro to the base level set.	
20	Ratio_zd	Ratio of level set at z=0 to base level set.	
21	Gradient_Magnitude	Magnitude of the gradient of the level set values.	
22	Period_Product	Product of periodicity parameters (NDr×NDang×NDax).	
23	Radial_Axial_Ratio	Ratio of radial periodicity (NDr) to axial periodicity (NDax).	
24	ri_Scaled_Levelset	Scaled level set value based on the inner radius (ri×baseLevelset).	
25	Porosity_TPMSAs_Ratio	Ratio of porosity to TPMS surface area.	

The predictive models were developed to evaluate two key responses: the temperature difference between the TPMS wall and the fluid region (ΔT_{wv}), as explained in section 2.4, and the friction factor. Using ΔT_{wv} and other parameters, the volumetric Nusselt number was calculated. However, the Nusselt number was not directly used as a response in the predictive model to ensure more accurate predictions.

Feature importance tests were conducted for each type of geometry using three different methods: ReliefF, Pearson correlation, and Spearman correlation. ReliefF evaluates feature importance by distinguishing nearby instances, considering relevance and redundancy. Pearson correlation measures linear relationships, while Spearman correlation assesses rank-based monotonic relationships, making it robust to non-linear dependencies. For the gyroid type specifically, the feature ranking results obtained from these three methods are illustrated in Figures 2.6A and 2.6B, with ΔT_{wv} as the response in Figure 2.6A and the friction factor as the response in Figure 2.6B.

For friction factor, features like $NDax$, dh, and $PorosityTPMSAs$ Ratio consistently rank high across all methods, indicating their strong linear and monotonic relationships, as well as their relevance in distinguishing nearby instances. Similarly, for $DeltaTwv$, features such as $TPMSAs$, Period Product, and $NDax$ emerge as universally significant. ReliefF highlights additional features like $NDang$ and NDr, emphasizing their importance in capturing local instance-based distinctions, which may be overlooked by correlation-based methods. Across both responses, feature like ri Scaled Level set consistently rank low, suggesting limited predictive utility.

Normalization aligns feature scales to improve model performance. Common methods include Min-Max Scaling, Robust Scaling, and Z-score Standardization. Z-score is preferred as it standardizes features to a mean of 0 and a standard deviation of 1, making it effective for datasets with normal distribution and suitable for many machine learning models.

2.5.4 Train Predictive Models

Various machine learning models were applied to the datasets. Gaussian Process Regression (GPR) models generally performed better and were employed with different kernels such as Rational Quadratic, Exponential, and Matern 5/2, tailored to the response variable types (ΔT_{wv} and f). The choice of kernel was determined based on the model's performance metrics.

To evaluate the models, a K-fold cross-validation method was used, ensuring that the data was not split into separate training and testing sets. Instead, the entire dataset was utilized in multiple folds, providing robust validation metrics. Using this approach, the Validation RMSE and R^2 values were computed.

As this study involves many features, a feature importance test was conducted to evaluate the relevance of each feature, as explained in the previous sections. However, selecting the optimal number of features and defining a minimum correlation threshold is a complex process that significantly affects the accuracy of machine learning models. To address this challenge, the number of features was systematically varied, starting from the top-ranked feature up to the 25th-ranked feature for each type of geometry and each response variable. This process was repeated using different machine learning models to ensure thorough evaluation and optimization. For example, in the case of the gyroid geometry and the Pearson method, as illustrated in Figure 2.7, the validation RMSE and R^2 were plotted against the number of features ranked by three different methods of feature importance. The Feature test is done for each Rational Quadratic, Exponential, and Matern 5/2, for different types of geometry and feature ranking methods, the best methods in terms of R^2 are picked as best performing model and summarized in Table 2.4.

Table 2.4 Optimized Machine Learning Models and Feature Importance methods for each geometry Type based on Response, with reported R squared and Number of Features required out of 25.

Type	Response	Ranking Method	Kernel	R^2	Number of Features
d	ΔT_{wv}	Pearson	Rational Quadratic	0.93	25
d	f	ReliefF	Exponential	0.97	21
g	ΔT_{wv}	Pearson	Rational Quadratic	0.85	11
g	f	Pearson	Exponential	0.97	12
n	ΔT_{wv}	ReliefF	Matern 5/2	0.93	18
n	f	Spearman	Exponential	0.83	10
p	ΔT_{wv}	Pearson	Exponential	0.93	15
p	f	Pearson	Exponential	0.92	24

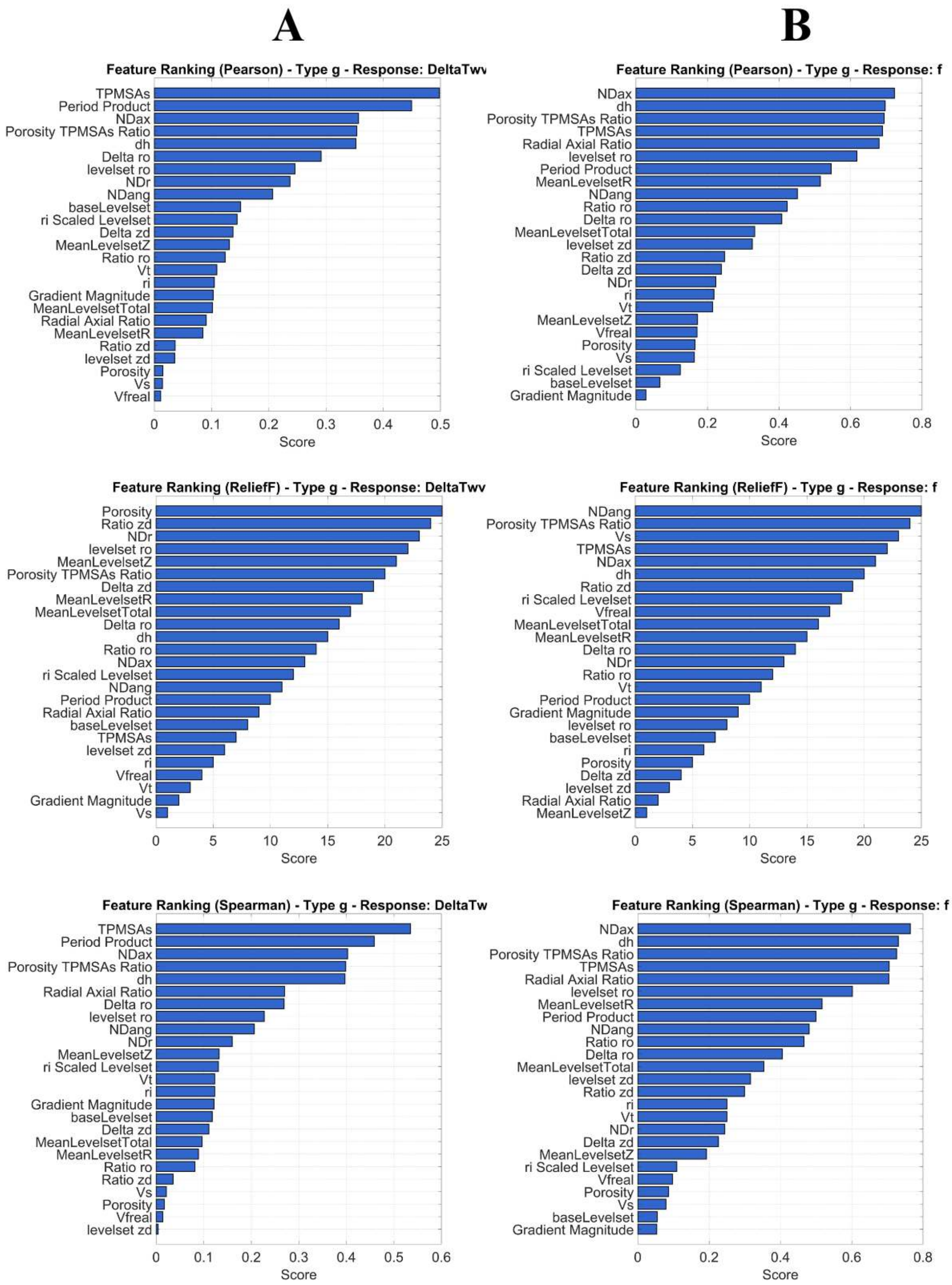

Figure 2.6 Feature Ranking for Gyroid Structure Using Three Methods (Pearson, ReliefF, Spearman). (A) Response DeltaTwv. (B) Response f.

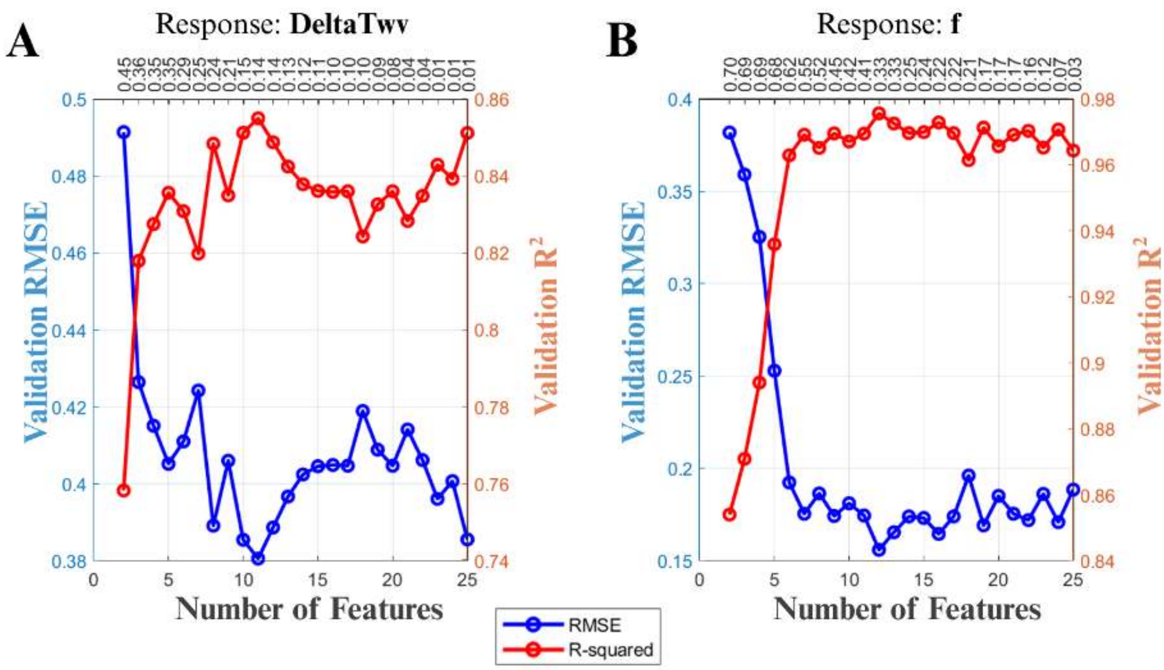

Figure 2.7 Feature Independence Plots. (A) Response: DeltaTwv. (B) Response: f.

2.6 *Optimization Algorithms*

The optimization of TPMS structures is challenging due to their complexity, defined by seven input parameters, including categorical variables like geometry type, and the conflicting nature of performance metrics, such as heat dissipation versus pressure drop. To address these challenges, evolutionary genetic algorithms were employed for their ability to handle categorical variables and effectively balance multi-objective trade-offs. Both direct and indirect genetic algorithms are utilized in this study to optimize TPMS structures and analyze the relationships between input parameters and performance metrics and finding optimum pareto fronts.

2.6.1 *Direct Genetic Algorithm Optimization*

The workflow of the Direct Genetic Algorithm optimization is illustrated in Figure 2.8, while the input parameters are detailed in Table 2.1. Among the eight inputs, seven are continuous variables with defined ranges, and one is categorical, representing the TPMS structure type. The population size was set to 80, considering the computational intensity of CFD simulations required to evaluate the performance metrics, which serve as the objective functions. Although a larger population size could enhance diversity and improve the exploration of the solution space, it would significantly increase computational time. Therefore, a population size of 80 was deemed reasonable for balancing computational feasibility and optimization efficiency.

The built-in multi-objective genetic algorithm in MATLAB was employed as a black-box tool to find the optimum for objective functions. The workflow begins with the generation of the initial population based on the defined ranges and proceeds with the evaluation of each individual using a live link between COMSOL and MATLAB. The evaluation process consists of two stages: meshing and calculating intermediate parameters (defined in Table 2.3), followed by running CFD simulations to obtain essential results for calculating the volumetric Nusselt number and friction factor. In this direct method, the fitness function is a MATLAB function integrated with COMSOL, directly using CFD results to evaluate the objectives. The optimization aims to maximize the volumetric Nusselt number (Nu_v) and minimize the friction factor (f). To convert this into a minimization problem and ensure comparable scales, the objectives are defined as ($-Nu_v$, $1000 \times f$).

The stopping criteria for the algorithm are set to terminate when the difference between objective values within a generation falls below 10^4 or when the maximum number of generations, set to 30, is reached. The entire optimization process required approximately 400 hours to complete 30 generations. All data and iterations were recorded for subsequent analysis. The Pareto fraction was set to 0.35, and the NSGA-II algorithm was used to generate the Pareto-optimal solutions.

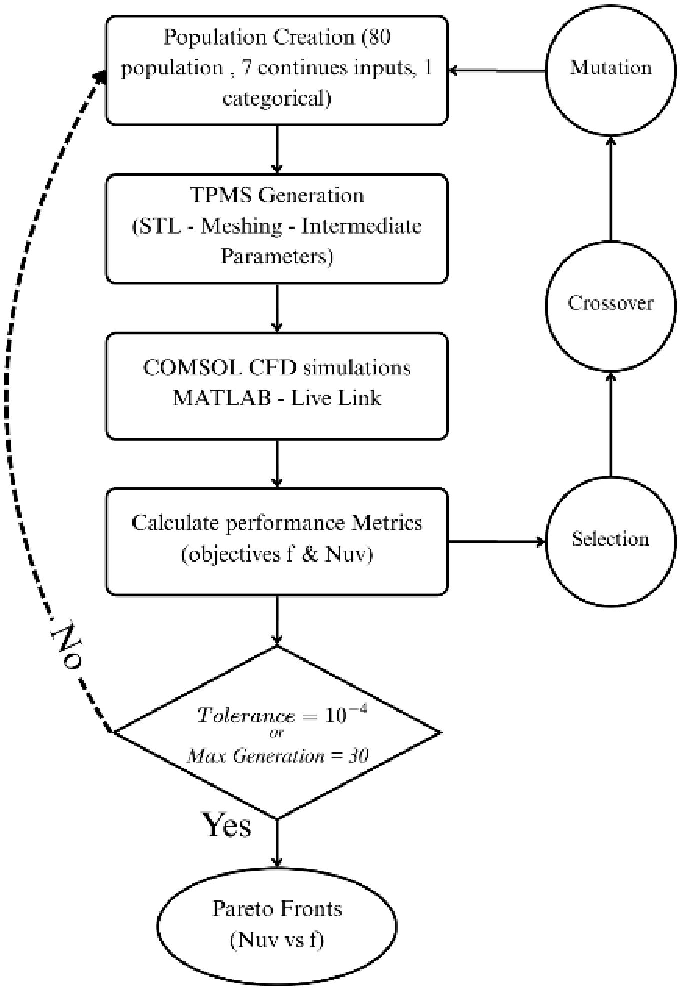

Figure 2.8 Workflow of Direct Genetic Algorithm Optimization. The workflow illustrates the method used in section 2.6.1.

2.6.2 In-Direct Genetic Algorithm Optimization

The workflow of the In-Direct Genetic Algorithm optimization which illustrated in Figure 2.9. Unlike the direct method, which relies on CFD simulations for every individual in the population, making it computationally expensive and time-consuming, the In-Direct method proposed in this study estimates the objectives using machine learning models described in Section 2.5. These machine learning models were trained using the data recorded during the Direct Genetic Algorithm optimization process. Like the direct method, the workflow begins with the generation of an initial population of 80 individuals, consisting of seven continuous inputs and one categorical input representing the type of geometry. The evaluation step, however, differs. In this method, COMSOL is used only for meshing the domains and calculating intermediate parameters such as porosity, hydraulic diameter, and surface area of the TPMS structure. Using the eight input variables and the evaluated intermediate parameters, additional features are created to enhance the prediction accuracy of the machine learning models. In total, 25 features are generated, as previously shown in Table 2.3. The process of feature selection, ranking, and its methodology is detailed in Section 2.5. The predicted friction factor (f) and the calculated volumetric Nusselt number (Nuv, derived from ΔTwv) are then used as the objective functions for the Genetic Algorithm. The optimization process continues until either the stopping criteria are met, or the maximum number of generations (30) is reached. This method significantly reduces computational time, completing the optimization within 22 hours compared to the 400 hours required by the direct method. The Pareto fronts generated from this process provide optimal trade-offs between the objectives.

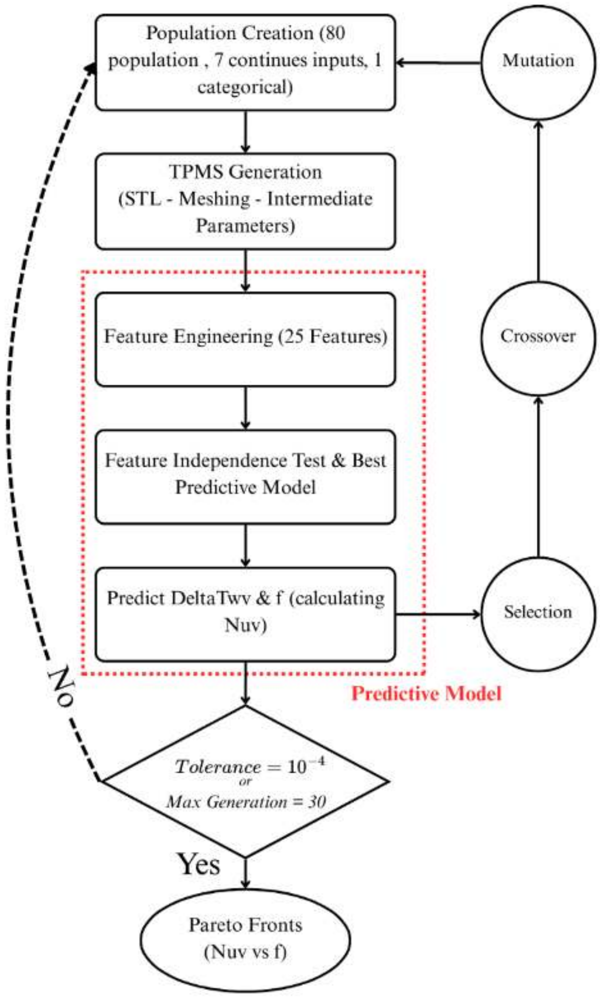

Figure 2.9 Workflow of In-Direct Genetic Algorithm Optimization. The workflow illustrates the method used in section 2.6.2.

Chapter 3:
RESULTS

This section presents the findings of the study, including the results and discussion related to the predictive models trained for estimating objective functions. It also covers the optimum solutions obtained from the Genetic Algorithm for both the direct and indirect methods, along with a comparison of their performance. Additionally, the analysis of CFD results is provided, focusing on the flow distribution, critical areas in terms of hydraulic and thermal performance, and their implications for TPMS structures.

3.1 Predictive Models

The development and training of predictive models, along with the selection of feature combinations based on feature importance tests, are thoroughly detailed in Section 2.5 of this study. The chosen machine learning models were selected based on their performance metrics, such as R^2, and were tailored to the type of geometry and the specific response variable (either f or ΔTwv). The R^2 values and the final selected models for each geometry type and response are summarized in Table 2.4. Additionally, the parity plots illustrating the performance of each model for each geometry type and response variable are presented in Figure 3.1.

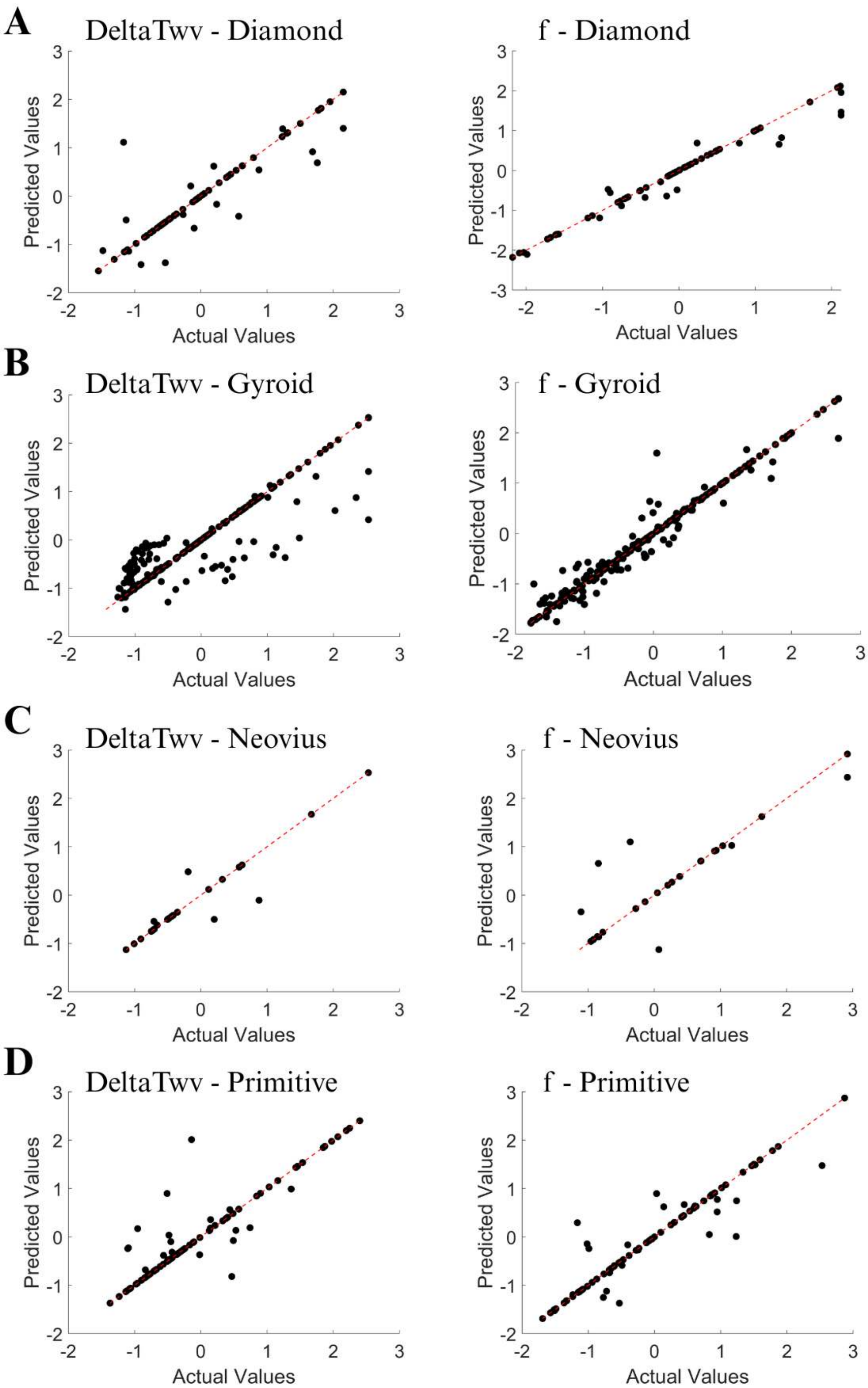

Figure 3.1 Parity Plots for Machine Learning Predictions. (A) DeltaTwv and f as responses for Diamond type. (B) DeltaTwv and f as responses for Gyroid type. (C) DeltaTwv and f as responses for Neovius type. (D) DeltaTwv and f as responses for Primitive type, comparing predicted versus actual values.

3.2 *Multi Objective Optimization*

The multi objective genetic optimization conducted for finding the optima solutions, finding the trade-off between objectives especially optimum pareto fronts.

3.2.1 Direct multi-objective optimization

As explained in Section 2.6.1, the multi-objective genetic algorithm was executed for 30 generations, with non-dominated optimum solutions presented as Pareto fronts in Figure 3.2. The objectives considered were the volumetric Nusselt number (N_{uv}) and the friction factor (f), with different TPMS geometries represented by distinct shapes. These results were obtained after approximately 400 hours of computation, with each generation consisting of 80 individuals and requiring 30 up to 50 minutes per evaluation. Notably, the maximum volumetric Nusselt number (Nu_v) achieved after 30 generations (Overall 2400 iterations) reached 1500, representing a 300% increase compared to the first generation's maximum Nu_v.

Although the algorithm could have continued until the tolerance criteria were met, the optimization process was terminated after 30 generations due to the high computational cost. Consequently, the Pareto front presented in Figure 3.2 may not represent the absolute optimum solutions and could be further improved with additional iterations.

Among the TPMS geometries, the gyroid type dominated the Pareto-optimal solutions, appearing most frequently. Only one diamond-type geometry appeared in the mid-trade-off region, while other types, such as Neovius and Primitive, were largely outperformed during the optimization process and their frequency dropped to zero by the end of the 30 generations. This indicates that gyroid structures exhibit superior performance in the trade-off between hydraulic and thermal metrics.

3.2.2 In-Direct multi-objective optimization

As described in Section 2.6.2, the in-direct optimization method replaces the computationally expensive CFD-based evaluations with predictions made by machine learning models. These models were trained using data obtained from the Direct Genetic

Algorithm. To enable a fair comparison with the direct method, the maximum generation size and tolerance conditions were set to be the same for both methods.

This in-direct approach significantly reduced computational time, completing 30 generations in approximately 30 hours, as opposed to the 400 hours required for the direct method. The resulting Pareto-optimal solutions are presented in Figure 3.2.

The Pareto front in Figure 3.2 illustrates the optimal trade-offs between the objectives (volumetric Nusselt number and friction factor). Notably, in the case of cylindrically arranged TPMS structures, the in-direct optimization resulted in a Pareto set that included Diamond type frequency more than Gyroid but still dominated other two types.

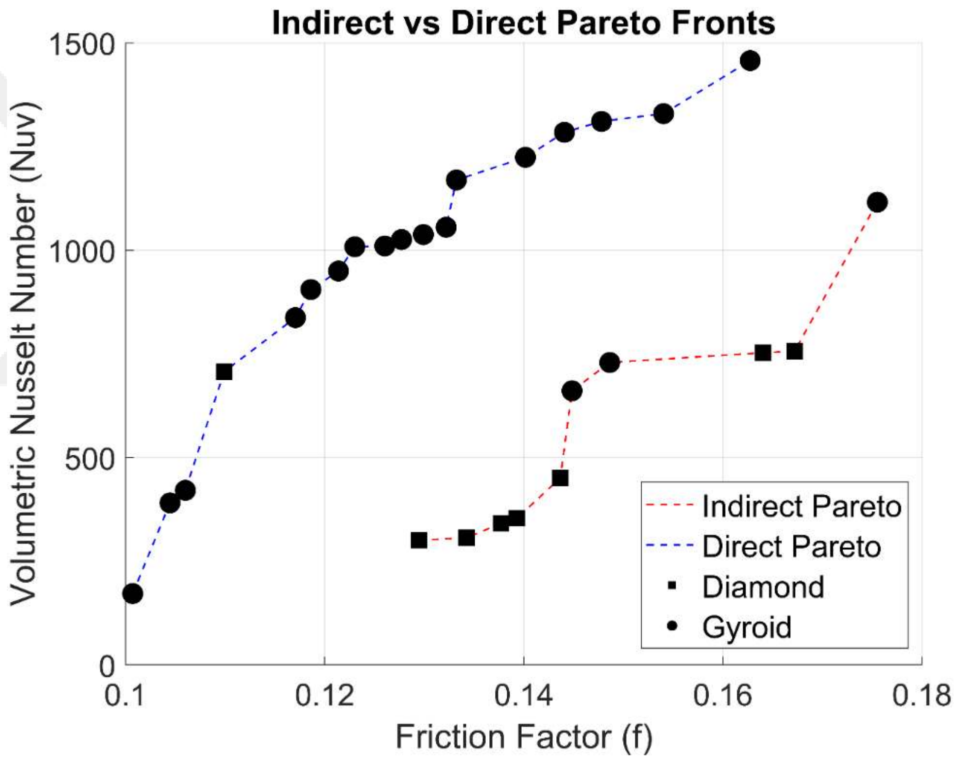

Figure 3.2 Pareto Fronts of Genetic Algorithm for Both Direct and In-Direct Methods.

3.2.3 Distribution pattern of pareto solutions

This section analyzes Figure 3.2 and Figure 3.3, which presents dot plots of Pareto solution distributions for each optimization input parameter under both Direct and In-Direct methods, to identify the parameter ranges most favorable in the $Nuv - f$ trade-off.

I. Distribution Pattern for Porosity

Figure 3.3 shows that the Pareto solutions cover porosity 0.30-0.60 but mostly cluster at 0.50-0.60. All Gyroid cases appear only at the higher porosity end (about 0.50-0.60), while all Diamond cases lie lower (about 0.35-0.50). This split is due to how each structure balances heat transfer and flow resistance. At higher porosity the Gyroid's smooth, continuous channels give good, wetted surface and gentle mixing without causing a large rise in friction, so the ratio of volumetric Nusselt number Nuv to friction factor f is favorable. When porosity gets smaller, the Gyroid passages become more tortuous and f increases faster than the gain in Nuv, so it is no longer optimal. The Diamond geometry, on the other hand, creates more small flow disturbances (accelerations, tiny recirculation zones) at lower porosity that help refresh the thermal boundary layer and raise Nuv enough to justify the added f in that range. At higher porosities, the Diamond structure loses effectiveness because the small-scale mixing effects become weaker and its available surface area is not utilized efficiently. As a result, Diamond designs no longer appear in the optimal set. In contrast, the Gyroid maintains strong performance in this range, making it the preferred geometry at high porosity, while Diamond remains the more competitive option at lower porosity.

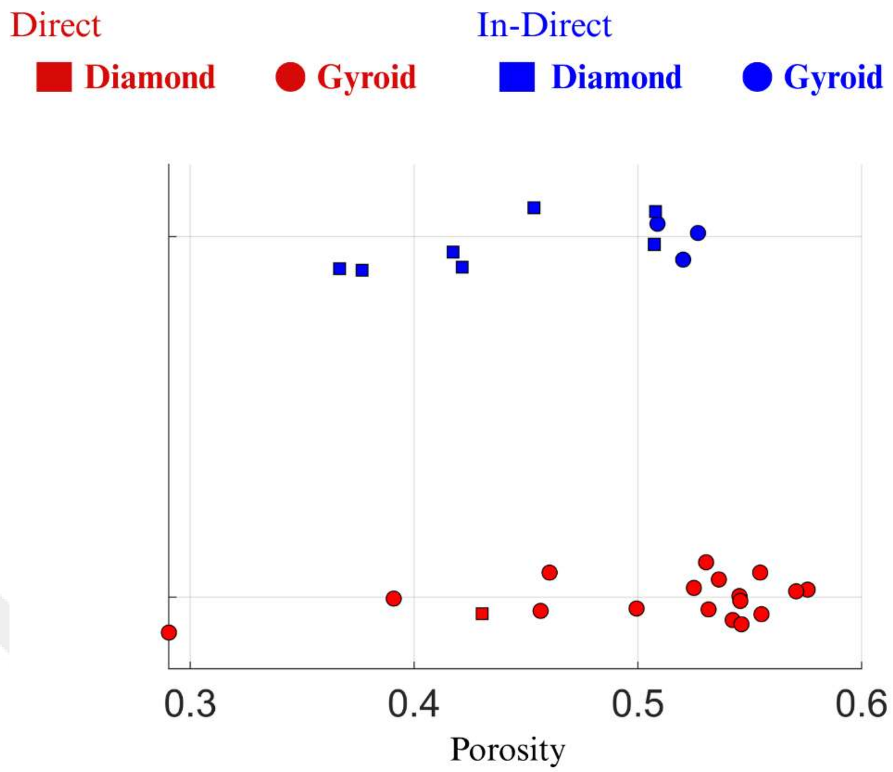

Figure 3.3 Distribution Pattern of Porosity Values in Pareto Solutions. Comparison of porosity distributions for In-Direct (upper set of points) and Direct (lower set of points) methods, with geometry types categorized by shapes (Diamond and Gyroid).

II. ***Distribution Pattern for r_i***

While the genetic algorithm permitted inner radius (r_i) values as low as 0.05 mm, but Figure 3.4 shows that the Pareto set starts at about 0.10 mm, so very small r_i values were not favored. This likely happens because the inlet jet first strikes the center of the cylindrical TPMS region; a larger inner radius there gives the flow more space to turn and spread, lowering the local pressure drop. The downside is that extra open space can carry less solid material for heat spreading and may lower temperature uniformity versus outer regions. Still, the optimal designs lean toward larger r_i. In the plot, Direct solutions cluster mostly above 0.18 mm (and overall, within roughly 0.16-0.18 mm, so they show less variety), while the In-Direct method keeps a broader spread. Overall, the algorithm converged on moderate-to-large inner radii because they balance easier inlet flow with acceptable thermal performance.

III. Distribution Patterns for Gradients of Level Set

The radial Level Set gradient $(Gradient\ R = LevelSet\ ro - LevelSet\ ri)$. A positive value means the structure becomes denser (lower porosity) outward; a negative value means porosity increases outward. In Figure 3.4 the Direct method Pareto solutions cluster mainly between -0.2,0, so they favor small, mostly slightly negative gradients. This happens because a mild outward increase in porosity lets the inlet flow turn and expand with lower pressure drop, keeps enough surface area for heat transfer, avoids strong radial temperature imbalance, and prevents the friction penalties of large positive gradients or the heat-transfer loss from very negative gradients. Also, the Direct method links gradient changes to other features, so extreme gradients tend to harm multiple objectives and are filtered out early. In contrast, the In-Direct method distributes solutions more evenly across the ri range.

The Axial Level Set gradient ($Gradient\ Z = LevelSet\ Zdown - LevelSet\ Ztop$). A positive value means the structure gets denser (porosity decreases) moving upward toward the inlet; a negative value would mean porosity increases upward. All Pareto-optimal solutions in both methods have a positive axial gradient, so the inlet region is more open, and the material becomes denser downstream. This open-dense sequence lowers entrance pressure losses (the inlet zone is most sensitive), lets the flow expand and stabilize before encountering tighter passages, and then uses the denser downstream region for added surface area and mixing, improving heat transfer without a large initial friction penalty. The Direct method spans a wider gradient range and includes many high values (often greater than 1), while the In-Direct method remains below about 0.8. High positive axial gradients are favored (unlike in the radial direction) because axial staging from open to dense aligns pressure and thermal objectives: early low resistance then later intensified convective area.

The three parameters $NDax, NDang, NDr$ denote the inverse of the number of unit cells in the axial, angular, and radial directions ($ND = \frac{1}{Ncells}$); thus, lower ND means more cell repetitions in that direction. The optimization range for $NDax$ was 0.2-1 (i.e. 5 down to 1 axial cells). In the Direct method the Pareto points cluster at $NDax \approx 0.2 - 0.3$ and $NDax \approx 0.2 - 0.3$ (about 3–5 axial layers), showing a consistent preference for a higher axial cell count because this increases internal surface area, repeatedly re-starts thermal boundary layers and still keeps the incremental pressure drop acceptable (shorter axial pitch avoids large abrupt contractions). The In-Direct method also favors low $NDax$ but spreads more widely. For $NDang$, the Direct solutions concentrate at low values corresponding to roughly 10 angular cells: many circumferential repetitions fragment the incoming flow into multiple slender streams, equalize distribution, reduce large-scale recirculation pockets, and enhance lateral thermal uniformity, while the added wetted perimeter boosts area-based performance with only a moderate friction penalty. In contrast, NDr concentrates at high values (1 to at most 2 radial cells), meaning the designs avoid excessive radial partitioning. Fewer radial cells avoid narrow high-loss annuli and stagnation, while many axial/angular cells raise area and keep flow uniform maximizing heat transfer per pressure drop.

3.3 CFD Results for Pareto Solutions

This section presents CFD contour plots of convective heat flux (W/m^2), magnitude Velocity ($\frac{m}{s}$), Temperature (K), and flow streamlines for selected Pareto-optimal TPMS designs taken from different regions of the Pareto front. The solutions chosen from both the indirect and direct methods are listed in Table 3.1, which also points to the related figures. Figures 3.5 (Gyroid) and 3.6 (Diamond) show the convective heat flux contours. Figure 3.7 and 3.8 show the Velocity and Temperature contours (A for Gyroid and B for Diamond). For each design, three views are provided: Case I is a vertical mid-plane section; Case II is a horizontal plane 0.4 mm above the bottom surface; and Case III is a horizontal plane 0.2 mm above the bottom surface. The specific sectional planes and their locations within the TPMS structure are illustrated in Figure 3.5. The goal is to compare how heat transfer and flow patterns change inside the structures.

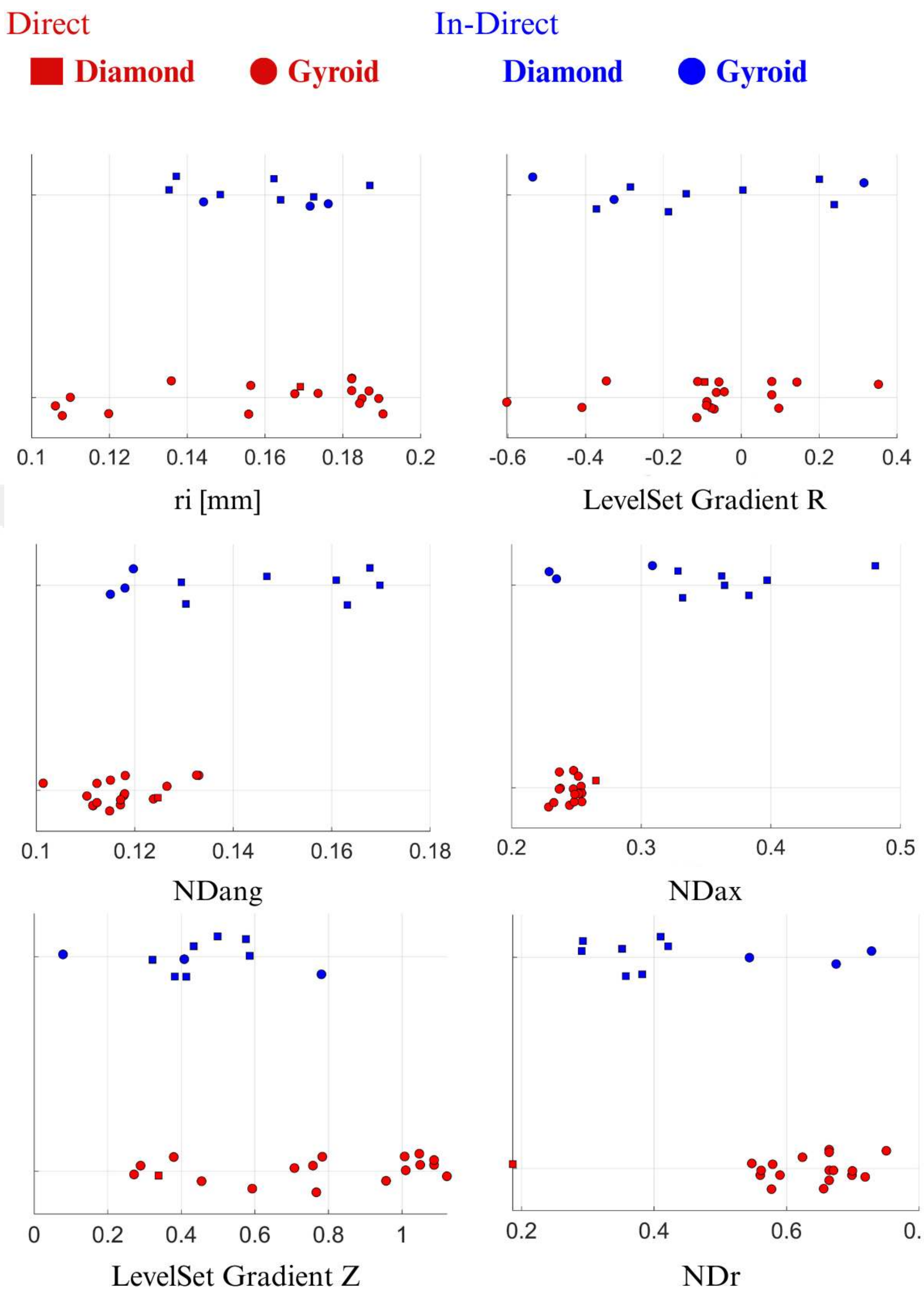

Figure 3.4 Distribution Pattern of inner radius, Values in Pareto Solutions. Comparison of porosity distributions for In-Direct (upper set of points) and Direct (lower set of points) methods, with geometry types categorized by shapes (Diamond and Gyroid).

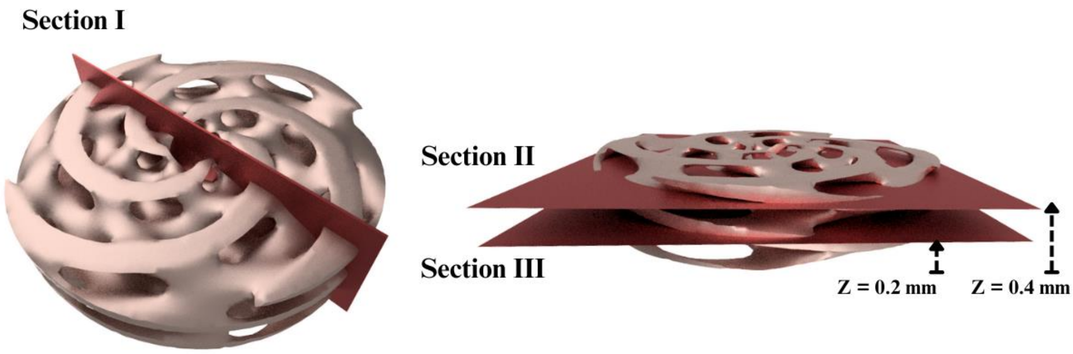

Figure 3.5 Section planes used in presenting CFD results: Case I is a vertical mid plane section; Case II is a horizontal plane 0.4 mm above the bottom surface; and Case III is a horizontal plane 0.2 mm above the bottom surface.

Table 3.1 Pareto Front Solutions for CFD Analysis

Figure	*Type*	*ri*	*Porosity*	*GradientR*	*Gradient Z*	*NDr*	*NDang*	*NDax*	Nu_v	*f*
3.5A	g	0.18	0.29	-0.6	0.59	0.71	0.11	0.25	166	0.1
3.5B	g	0.1	0.57	-0.08	0.37	0.57	0.13	0.23	1268	0.15
3.6A	d	0.16	0.42	-0.09	0.33	0.18	0.12	0.26	699	0.1
3.6B	d	0.17	0.36	-0.37	0.43	0.35	0.16	0.48	106	0.14

3.3.1 Pareto solutions for Gyroid

Two Pareto-optimal gyroid cases were selected to illustrate the trade-off between heat transfer and pressure loss. Case A represents a solution with relatively low Nusselt number (Nu_v) and low friction factor (f). Case B represents a solution with high Nu_v and high f.

Case A (Figure 3.6.A: Views I–III)

In Case A the porosity is higher at the top and decreases sharply toward the bottom due to a strong negative gradient in the Z direction.

View I (vertical section) show that the gyroid channels become tighter toward the lower region. This rapid reduction in local Porosity weakens lateral flow connectivity in the lower part of the structure. As a result, part of the internal surface is less effectively swept by the fluid, which lowers local heat transfer and reduces the overall effective surface.

The gyroid passages are not straight; their wavy and interconnected form can promote mixing and support heat transfer in the upper and mid regions. However, when the constriction becomes too strong, it may also create zones of low velocity or stagnation and increase pressure drop without proportional thermal benefit.

View II (near-top horizontal cut) shows a relatively uniform distribution of the incoming flow. The inlet stream divides into approximately nine sub-channels. This division corresponds to the angular discretization parameter $NDang \approx 0.11$, giving about $1 / 0.11 \approx 9$ angular cells. Flow spreading at this level is still effective. View III (lower horizontal cut) shows that vertical connectivity remains, but lateral inter-layer connectivity has diminished. The tightening geometry restricts cross-level exchange and limits deeper penetration of the flow.

Case B (Figure 3.6.B: Views I–II)

In Case B the axial porosity gradient is weaker. Porosity still decreases from top to bottom, but more gradually than in Case A.

View I (vertical section) show that the channels maintain better continuity along the Z direction. This sustains flow connectivity into the lower regions, enabling more of the internal surface to participate in convective heat transfer. The maintained connectivity explains the higher Nusselt number observed for this case, though it comes with a higher friction factor.

View II (near-top horizontal cut) again shows a reasonably uniform flow distribution. Here the inlet divides into about eight sub-channels, consistent with $NDang \approx 0.13$ $(1 / 0.13 \approx 8)$. The slightly larger $NDang$ value (compared to Case A) yields fewer angular cells. Despite that, the distribution remains even.Figures 3.8A and 3.9A display the velocity and temperature contours for the Gyroid structure (Case B from Table 3.1). In Figure 3.8A, Section II reveals higher velocity spots in the areas between radially repeating cells, indicating enhanced mixing and improved heat transfer, though this comes with a consequent increase in pressure drop. As noted in previous sections, a greater number of radially repeated cells correlates with higher volumetric Nusselt numbers (Nu_v), and this contour plot supports that finding. In Figure 3.9B, the temperature contours demonstrate a predominantly uniform temperature distribution across the Gyroid structure, with only minor denser regions. This uniformity is attributed to the smooth, interconnected wavy channels.

3.3.2 Pareto solutions for Diamond

Two Pareto-optimal diamond where Case B represents a solution with relatively low Nusselt number (Nuv) and low friction factor (f). Case A represents a solution with high Nu_v and high f.

Case A (Figure 3.7.A: Views I–III)

View I show a diamond-type structure whose channels are mostly straight. The applied level-set gradient is low, so porosity changes are mild. This helps preserve both lateral and vertical connectivity of channels. In similar gradient conditions a gyroid can start to lose some of its connections, so this straightness is an advantage for diamond structure. The radial porosity gradient is set negative (by your convention this means porosity increases outward). Thus, the inner channels are narrower, and the outer channels are more open. The heat convection flux contours are intense near the center where the channels are tighter; this supports higher local velocities and higher local Nuv. This inward concentration of heat transfer helps raise the overall Nuv for the design.

View II (a near-top horizontal cut) shows that the inlet flow divides into about eight angular sub-channels. This matches the angular discretization parameter $NDang \approx 0.12$, since $1\ /\ 0.12\ \approx 8$ angular cells. Flow spreading is still effective at this plane. There is no clear loss of connectivity between View II and View III; the main paths stay continuous. The number of cells in the radial direction is relatively large: with a radial step of about 0.18 we have $1\ /\ 0.18\ \approx 5$, so effectively 5 radial layers. With both angular and radial repeats large, some channels start to bend and gain slight curvature instead of staying perfectly straight along the radial direction. This mild curvature can aid mixing without yet causing disconnection. Overall, in Case A the combination of preserved connectivity, moderate porosity gradient, and tighter inner passages supports a higher Nuv.

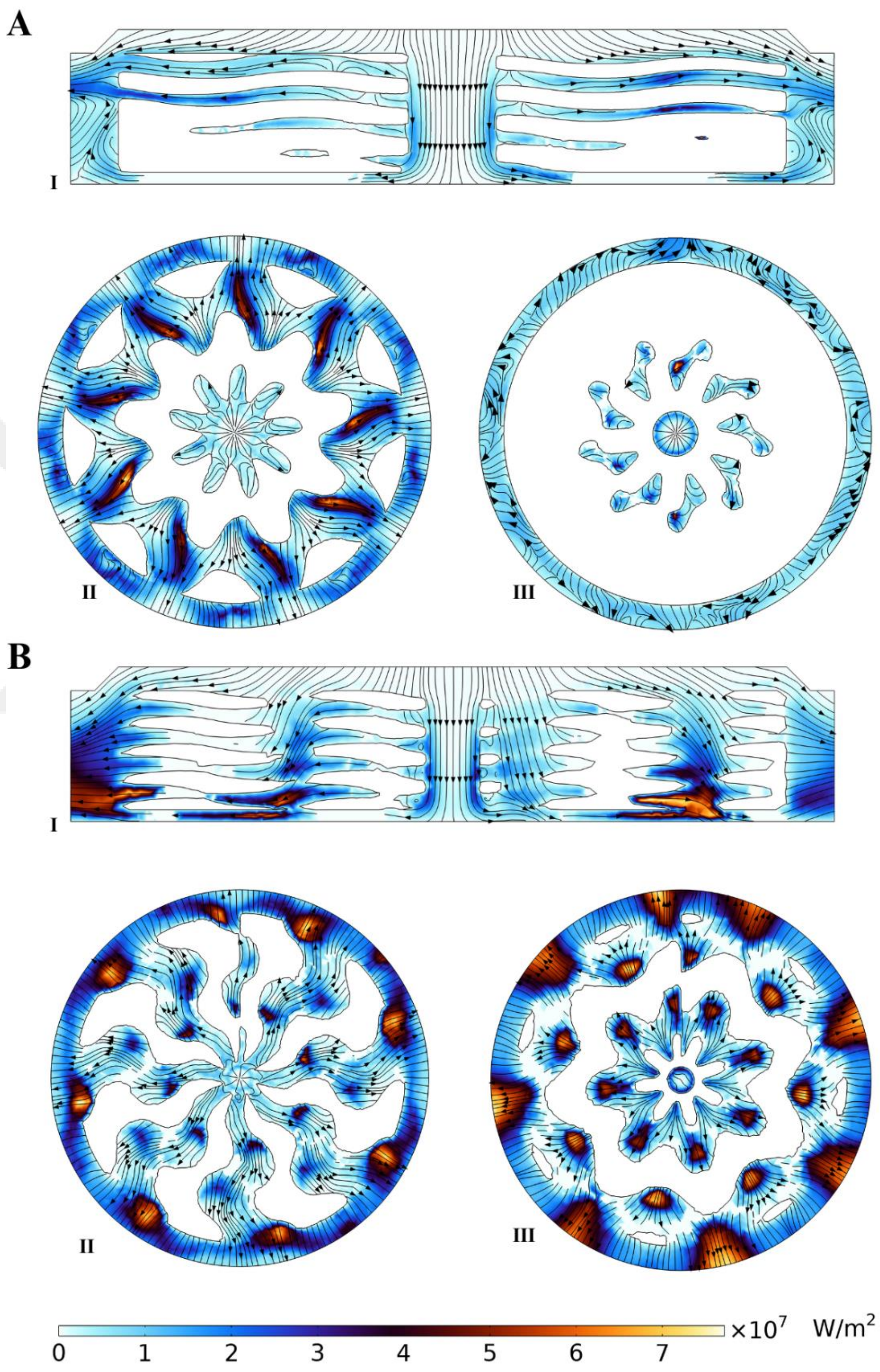

Figure 3.6 Convective Heat Flux Magnitude (W/m^2) Contours and Flow Streamlines for Candidate Pareto Solutions for Gyroid. (A) Case A of Table 3.1 (B) Case B of Table 3.1. Vertical midplane section (View I), horizontal plane 0.4 mm above the bottom (View II), and horizontal plane 0.2 mm above the bottom (View III)

Case B (Figure 3.7.B: Views I–II)

This shows stronger imposed gradients. The axial (Z) gradient is larger, and in View I (lower axial region) the structure has lower porosity. This reduces connectivity a little in both lateral and vertical directions near the bottom. There is also a negative radial gradient (again by your sign convention meaning porosity increases outward), so the outer region is more open than the inner region. However, in Case B the numbers of angular, axial, and radial repeats are all low. This limits the total internal surface area. With fewer repeating cells the effective area for convection is smaller, so the Nusselt number is lower. The slight loss of connectivity in the low-porosity bottom zone further reduces flow uniformity and the potential for heat transfer enhancement.

Figures 3.8B and 3.9B present the velocity and temperature contours for the Diamond structure (Case A from Table 3.1). In Figure 3.8B, Section I reveals a more uniform velocity distribution within the cells compared to the Gyroid, attributed to the Diamond's straight-sloped channels rather than wavy ones. This design results in fewer barriers for the fluid, maintaining a consistent velocity throughout the structure. In Figure 3.9B, the temperature contours show that Section I exhibits higher temperatures in the lower lateral areas compared to the rest of the structure. Unlike Gyroid, Diamond has a reduced ability to mix the fluid and generate vortices for heat dissipation. However, it excels in maintaining a pressure drop below a specific threshold, offering a different balance of thermal and hydraulic performance.

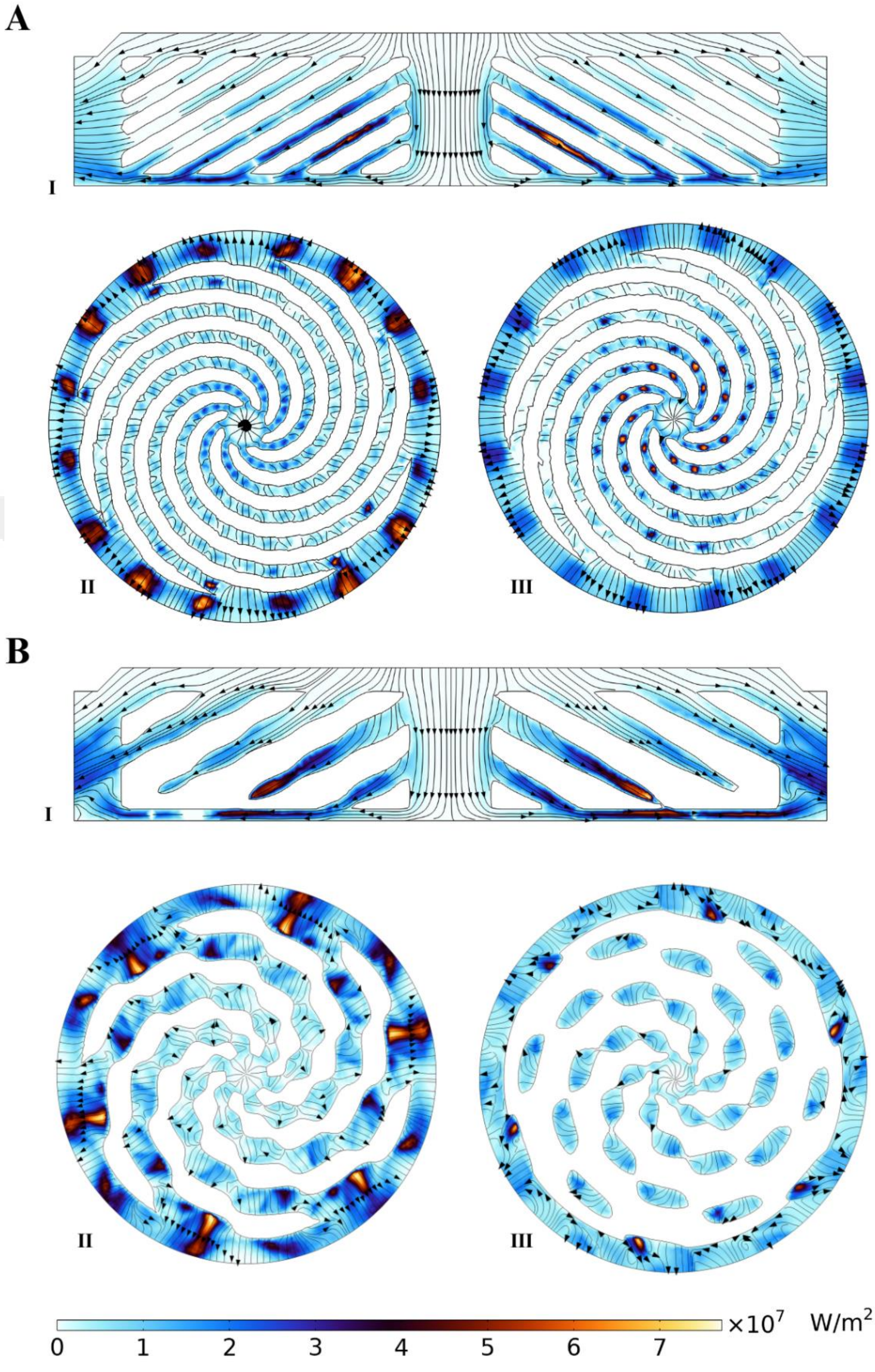

Figure 3.7 Convective Heat Flux Magnitude (W/m^2) Contours and Flow Streamlines for Candidate Pareto Solutions for Diamond. (A) Case A of Table 3.1 (B) Case B of Table 3.1. Vertical midplane section (View I), horizontal plane 0.4 mm above the bottom (View II), and horizontal plane 0.2 mm above the bottom (View III)

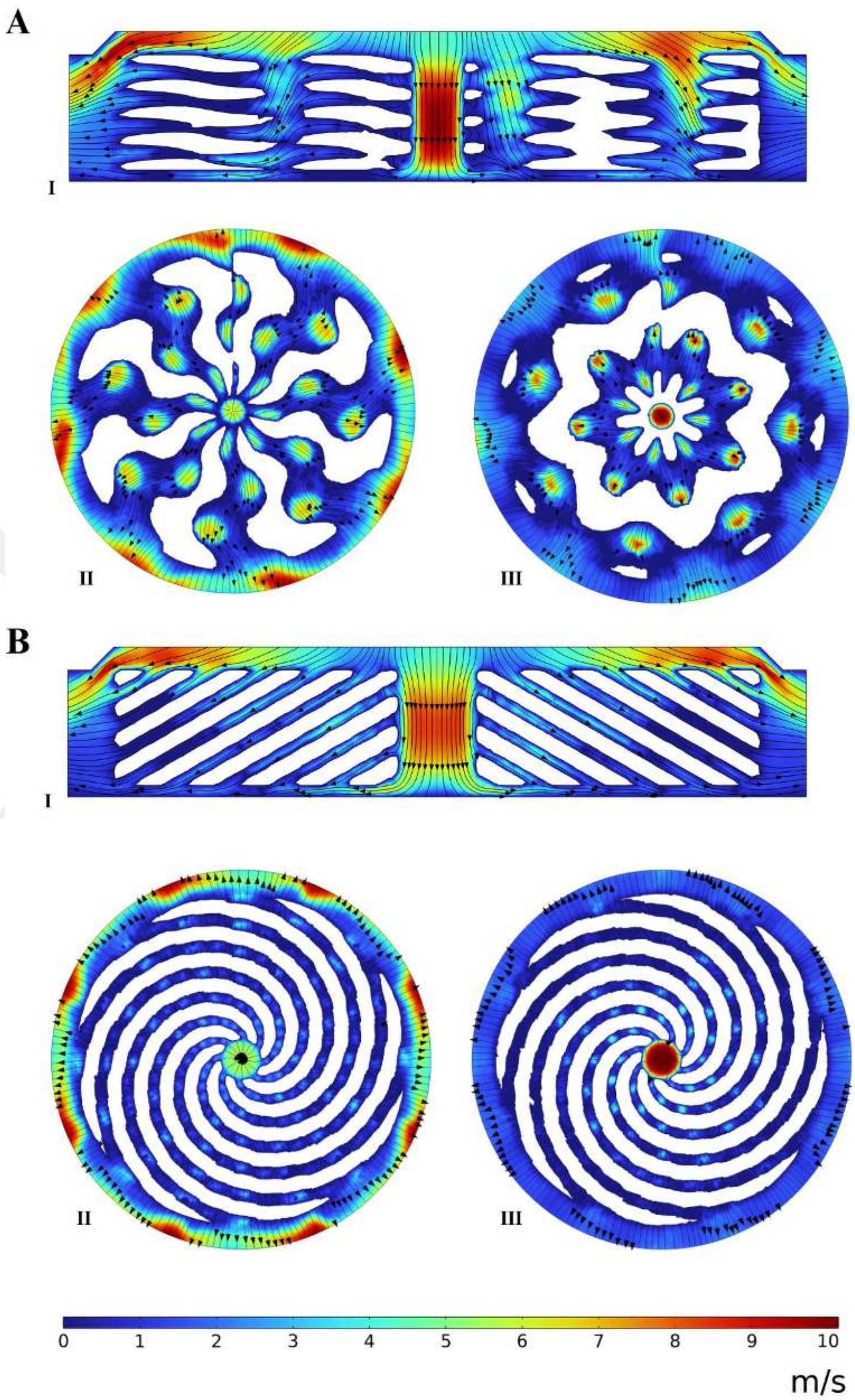

Figure 3.8 Velocity Magnitude ($\frac{m}{s}$) Contours and Flow Streamlines for Candidate Pareto Solutions. (A) Case B - Gyroid of Table 3.1 (B) Case A - Diamond of Table 3.1. Vertical midplane section (View I), horizontal plane 0.4 mm above the bottom (View II), and horizontal plane 0.2 mm above the bottom (View III)

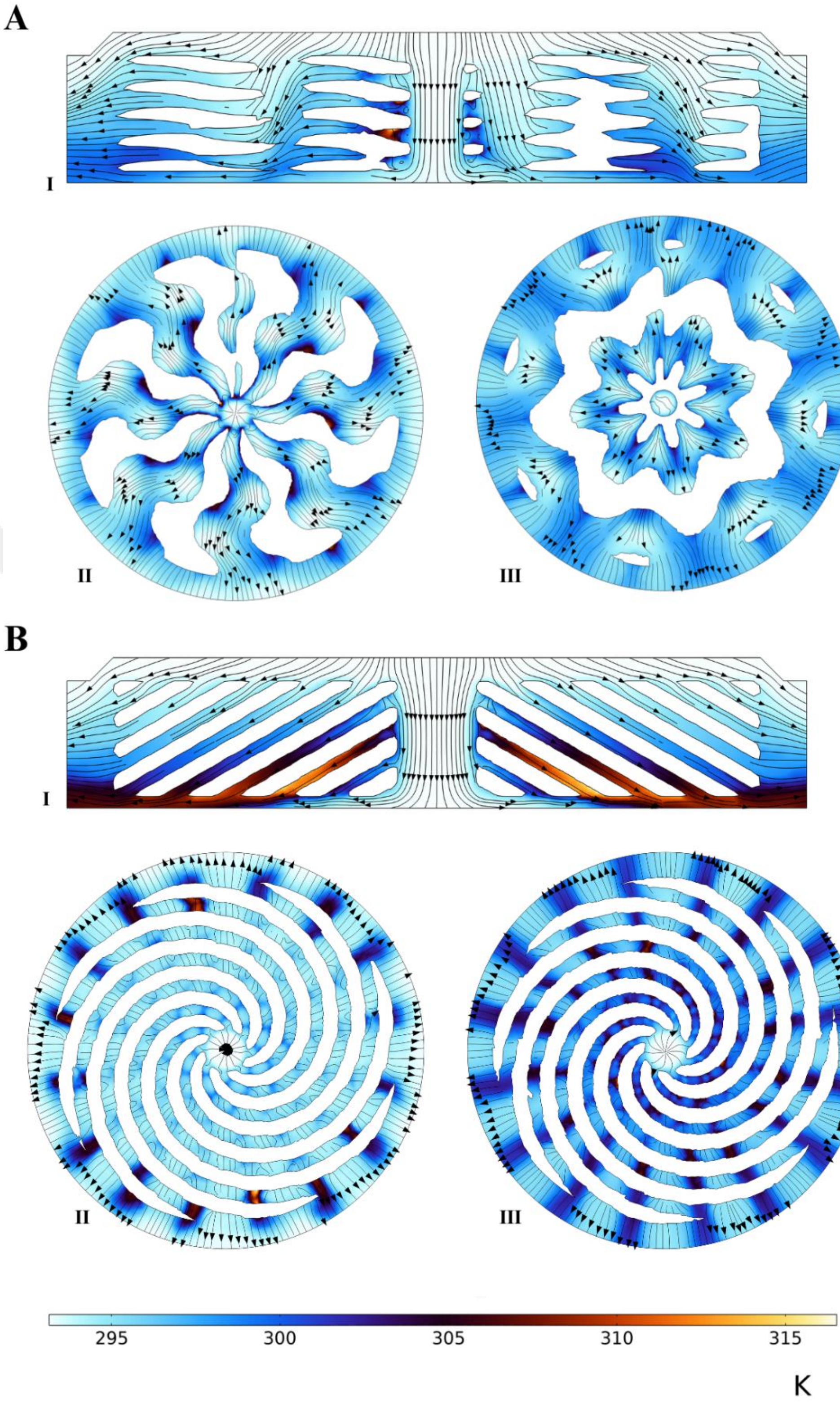

Figure 3.9 Temperature (K) Contours and Flow Streamlines for Candidate Pareto Solutions. (A) Case B - Gyroid of Table 3.1 (B) Case A - Diamond of Table 3.1. Vertical midplane section (View I), horizontal plane 0.4 mm above the bottom (View II), and horizontal plane 0.2 mm above the bottom (View III)

Chapter 4:

LIMITATIONS AND FUTURE WORK

4.1 *Limitations*

Although the optimization framework presented in this thesis demonstrates strong potential for advancing microscale thermal management, several limitations should be acknowledged. The study is entirely computational, and while the simulations were validated through accepted numerical approaches, experimental verification was not performed. As a result, the predicted thermal and hydraulic behaviors of the optimized TPMS structures remain to be confirmed under realistic operating conditions where fabrication imperfections, material anisotropies, and flow instabilities may arise. The geometrical design space was constrained to a subset of TPMS families and cylindrical arrangements, which, although beneficial for demonstrating the concept, excludes many possible structures and hybrid configurations that could further improve performance. The optimization process was also limited by computational cost, with the number of generations capped at thirty. This restriction may have prevented the algorithm from fully converging toward the global Pareto-optimal front. Similarly, the use of surrogate models, though effective in reducing computation time, was trained on a dataset biased toward structures that survived genetic selection, potentially limiting the generalizability of the predictions for less-explored regions of the design space. Boundary conditions, including fixed Reynolds number and heat flux, represent simplified operational scenarios that may not capture the variability of real cooling applications where transient loads, multiphase flow, or non-Newtonian coolants might alter system behavior.

4.2 *Future Work*

- Conduct experimental validation using additive manufacturing and thermo-hydraulic testing of optimized TPMS structures.
- Expand the design space to include additional TPMS families, hybrid structures, and nature-inspired geometries.
- Incorporate structural considerations such as thermal stresses, fatigue, and mechanical stability to ensure practical applicability.

- Extend the framework to transient conditions, non-uniform heating, and alternative coolants, including nanofluids and phase-change materials.
- Employ advanced machine learning and deep learning surrogates trained on systematically generated datasets to improve prediction fidelity.
- Develop multi-scale models linking pore-level geometry with device-scale performance for integration into full thermal management systems.
- Investigate manufacturability aspects such as tolerance to wall thickness variations, surface roughness, and porosity deviations that may affect robustness in practice.

Chapter 5:
CONCLUSION

- This study developed a multi-objective optimization framework for cylindrically arranged Triply Periodic Minimal Surface (TPMS) porous structures to enhance thermal and hydraulic performance in microscale thermal management. Key components included conjugate heat transfer simulations in COMSOL Multiphysics, coupled with genetic algorithms (GAs) and machine learning (ML) surrogates in MATLAB, optimizing seven geometric parameters including cell density, morphology, and level-set gradients to maximize volumetric Nusselt number (Nuv) while minimizing friction factor (f) across four TPMS types (gyroid, diamond, Neovius, primitive).
- Direct GA optimization over 30 generations (80 individuals) produced Pareto fronts dominated by gyroid structures, achieving up to 300% Nuv improvement with controlled f increases. Optimal parameter ranges included porosities of 0.50–0.60 for gyroids and 0.35–0.50 for diamonds, inner radii of 0.16–0.18 mm, positive axial gradients (0.3–0.8), and high axial/angular cell counts ($NDax \approx 0.23 - 0.25, NDang \approx 0.11 - 0.13$) with minimal radial partitioning ($NDr \approx 0.18 - 0.25$). Indirect GA, leveraging Gaussian Process Regression (GPR) models (R^2: $0.83 - 0.97$), reduced computational time from 400 to 30 hours, maintaining solution quality.
- Feature ranking via Pearson, Spearman, and ReliefF methods to identify the most influential variables. The analysis revealed that porosity, TPMS surface area, and periodicity products were the top-ranked features, each exhibiting strong correlations with the target variable (above 0.7). Notably, the ReliefF method effectively captured non-linear interactions.
- CFD analyses revealed gyroid designs with stronger axial gradients enhanced Nu_v via improved flow connectivity, while diamond structures excelled at lower porosities due to inward-concentrated heat flux. Streamlines confirmed uniform flow distribution ($\sim 8 - 10$ angular sub-channels), minimizing stagnation. The cylindrical arrangement outperformed cuboidal lattices in flow equalization, reducing hot spotsç

BIBLIOGRAPHY

[1] Y. Shabany, Heat Transfer, CRC Press, 2009. https://doi.org/10.1201/9781439814680.

[2] Z. He, Y. Yan, Z. Zhang, Thermal management and temperature uniformity enhancement of electronic devices by micro heat sinks: A review, Energy 216 (2021) 119223. https://doi.org/10.1016/j.energy.2020.119223.

[3] P. Lall, M.G. Pecht, E.B. Hakim, Influence of Tempemture on Microelectronics and System Reliability, CRC Press, 2020. https://doi.org/10.1201/9780138750879.

[4] B. Heidarshenas, A.S. El-Shafay, S.M. Sajadi, Y. Yuan, Enhancing efficiency in microscale systems with microchannels: a review, J Therm Anal Calorim 149 (2024) 11963–11988. https://doi.org/10.1007/s10973-024-13454-4.

[5] Z.-Y. Guo, Z.-X. Li, Size effect on single-phase channel flow and heat transfer at microscale, Int J Heat Fluid Flow 24 (2003) 284–298. https://doi.org/10.1016/S0142-727X(03)00019-5.

[6] P. Rosa, T.G. Karayiannis, M.W. Collins, Single-phase heat transfer in microchannels: The importance of scaling effects, Appl Therm Eng 29 (2009) 3447–3468. https://doi.org/10.1016/j.applthermaleng.2009.05.015.

[7] F. Chen, X. Jiang, C. Lu, Y. Wang, P. Wen, Q. Shen, Heat transfer efficiency enhancement of gyroid heat exchanger based on multidimensional gradient structure design, International Communications in Heat and Mass Transfer 149 (2023) 107127. https://doi.org/10.1016/j.icheatmasstransfer.2023.107127.

[8] I. El Khadiri, M. Abouelmajd, M. Zemzami, N. Hmina, M. Lagache, S. Belhouideg, Comprehensive analysis of flow and heat transfer performance in triply periodic minimal surface (TPMS) heat exchangers based on Fischer-Koch S, PMY, FRD, and Gyroid structures, International Communications in Heat and Mass Transfer 156 (2024) 107617. https://doi.org/10.1016/j.icheatmasstransfer.2024.107617.

[9] W. Tang, H. Zhou, Y. Zeng, M. Yan, C. Jiang, P. Yang, Q. Li, Z. Li, J. Fu, Y. Huang, Y. Zhao, Analysis on the convective heat transfer process and performance evaluation of Triply Periodic Minimal Surface (TPMS) based on

Diamond, Gyroid and Iwp, Int J Heat Mass Transf 201 (2023) 123642. https://doi.org/10.1016/j.ijheatmasstransfer.2022.123642.

[10] O.-R. Luis Guillermo, G.-O. Arturo, P.-B. James, P. Saul, Computational analysis and engineering modeling for the heat transfer and fluid flow through the gyroid TPMS structure, Appl Therm Eng 268 (2025) 125865. https://doi.org/10.1016/j.applthermaleng.2025.125865.

[11] M. Modrek, A. Viswanath, K.A. Khan, M.I. Hassan Ali, R.K. Abu Al-Rub, Multi-objective topology optimization of passive heat sinks including self-weight based on triply periodic minimal surface lattices, Case Studies in Thermal Engineering 42 (2023) 102684. https://doi.org/10.1016/j.csite.2022.102684.

[12] B. Hu, Z. Wang, C. Du, W. Zou, W. Wu, J. Tang, J. Ai, H. Zhou, R. Chen, B. Shan, Multi-objective Bayesian optimization accelerated design of TPMS structures, Int J Mech Sci 244 (2023) 108085. https://doi.org/10.1016/j.ijmecsci.2022.108085.

[13] R. Attarzadeh, S.-H. Attarzadeh-Niaki, C. Duwig, Multi-objective optimization of TPMS-based heat exchangers for low-temperature waste heat recovery, Appl Therm Eng 212 (2022) 118448. https://doi.org/10.1016/j.applthermaleng.2022.118448.

[14] C. Qian, J. Wang, X. Qiu, R. Ma, W. Xuan, B. Yu, J. Shi, J. Chen, Optimization design and heat transfer investigation of TPMS compact heat exchanger based on field synergy principle, International Communications in Heat and Mass Transfer 165 (2025) 109003. https://doi.org/10.1016/j.icheatmasstransfer.2025.109003.

[15] A. V. Anacreonte, M. Iasiello, G.M. Mauro, N. Bianco, W.K.S. Chiu, Pore-Scale multi-objective shape optimization of triply periodic minimal surface cellular architectures: Volumetric Nusselt number versus friction factor, Int J Heat Mass Transf 236 (2025). https://doi.org/10.1016/j.ijheatmasstransfer.2024.126318.

[16] T. Rehman, U. Sajjad, B. Lamrani, A. Shahsavar, H.M. Ali, W.-M. Yan, C.W. Park, Investigation on the thermal control and performance of PCM–porous media-integrated heat sink systems: Deep neural network modelling employing experimental correlations, Renew Energy 220 (2024) 119719. https://doi.org/10.1016/j.renene.2023.119719.

[17] Y. Li, B. Yang, L. Gong, W. Cui, Y. Yang, Machine learning prediction of thermo-hydraulic performance in gradient metal foam heat sink with

microencapsulated phase change material slurry, Int J Heat Mass Transf 253 (2025) 127610. https://doi.org/10.1016/j.ijheatmasstransfer.2025.127610.

[18] M.R. Shaeri, S. Sarabi, A.M. Randriambololona, A. Shadlo, Machine learning-based optimization of air-cooled heat sinks, Thermal Science and Engineering Progress 34 (2022) 101398. https://doi.org/10.1016/j.tsep.2022.101398.

[19] S.D. Farahani, A.J. Mamoei, A. Alizadeh, Thermal performance of microchannel heat sink integrated with porous medium, slip coefficient and phase change material and machine learning approach, J Energy Storage 74 (2023) 109357. https://doi.org/10.1016/j.est.2023.109357.

[20] B. Cao, Z. Wu, Microchannel heat sinks for hotspot thermal management: achieving minimal pressure drop and maximal thermal performance, Int J Heat Mass Transf 236 (2025) 126411. https://doi.org/10.1016/j.ijheatmasstransfer.2024.126411.

[21] D. Ansari, K.-Y. Kim, Hotspot thermal management using a microchannel-pinfin hybrid heat sink, International Journal of Thermal Sciences 134 (2018) 27–39. https://doi.org/10.1016/j.ijthermalsci.2018.07.043.

[22] Z. Soleymani, M. Rahimi, M. Gorzin, Y. Pahamli, Performance analysis of hotspot using geometrical and operational parameters of a microchannel pin-fin hybrid heat sink, Int J Heat Mass Transf 159 (2020) 120141. https://doi.org/10.1016/j.ijheatmasstransfer.2020.120141.

[23] D. Ansari, J.H. Jeong, A silicon-diamond microchannel heat sink for die-level hotspot thermal management, Appl Therm Eng 194 (2021) 117131. https://doi.org/10.1016/j.applthermaleng.2021.117131.

[24] X. Rao, C. Jin, H. Zhang, J. Song, C. Xiao, A hybrid microchannel heat sink with ultra-low pressure drop for hotspot thermal management, Int J Heat Mass Transf 211 (2023) 124201. https://doi.org/10.1016/j.ijheatmasstransfer.2023.124201.

[25] A. Tikadar, S. Kumar, Local hotspot thermal management using metal foam integrated heat sink, Appl Therm Eng 221 (2023) 119632. https://doi.org/10.1016/j.applthermaleng.2022.119632.

[26] K. M Moerman, GIBBON: The Geometry and Image-Based Bioengineering add-On, The Journal of Open Source Software 3 (2018) 506. https://doi.org/10.21105/joss.00506.

[27] J.W. Fisher, S.W. Miller, J. Bartolai, T.W. Simpson, M.A. Yukish, Catalog of triply periodic minimal surfaces, equation-based lattice structures, and their homogenized property data, Data Brief 49 (2023) 109311. https://doi.org/10.1016/j.dib.2023.109311.

[28] A. Jones, M. Leary, S. Bateman, M. Easton, TPMS Designer: A tool for generating and analyzing triply periodic minimal surfaces, Software Impacts 10 (2021) 100167. https://doi.org/10.1016/j.simpa.2021.100167.

[29] M. Vafaeefar, K.M. Moerman, T.J. Vaughan, LatticeWorks: An open-source MATLAB toolbox for nonuniform, gradient and multi-morphology lattice generation, and analysis, Mater Des 250 (2025) 113564. https://doi.org/10.1016/J.MATDES.2024.113564.

[30] K. Yan, J. Wang, L. Li, H. Deng, Numerical investigation into thermo-hydraulic characteristics and mixing performance of triply periodic minimal surface-structured heat exchangers, Appl Therm Eng 230 (2023) 120748. https://doi.org/10.1016/j.applthermaleng.2023.120748.

[31] C. Zeng, W. Wang, Modeling method for variable and isotropic permeability design of porous material based on TPMS lattices, Tribol Int 176 (2022) 107913. https://doi.org/10.1016/j.triboint.2022.107913.

[32] Z. Zhang, H. Zhang, J. Zhang, S. Qin, M. Duan, Study on flow field characteristics of TPMS porous materials, Journal of the Brazilian Society of Mechanical Sciences and Engineering 45 (2023) 188. https://doi.org/10.1007/s40430-023-04113-0.

[33] D. Ali, M. Ozalp, S.B.G. Blanquer, S. Onel, Permeability and fluid flow-induced wall shear stress in bone scaffolds with TPMS and lattice architectures: A CFD analysis, European Journal of Mechanics - B/Fluids 79 (2020) 376–385. https://doi.org/10.1016/j.euromechflu.2019.09.015.

[34] A. Tariq, Z. Liu, A pore-scale analysis for friction factor and permeability in confined porous medium with LB method, International Communications in Heat and Mass Transfer 127 (2021) 105559. https://doi.org/10.1016/j.icheatmasstransfer.2021.105559.

[35] L. wen Jin, K.C. Leong, Pressure drop and friction factor of steady and oscillating flows in open-cell porous media, Transp Porous Media 72 (2008) 37–52. https://doi.org/10.1007/s11242-007-9134-3.

[36] M.T. Pamuk, M. Özdemir, Friction factor, permeability and inertial coefficient of oscillating flow through porous media of packed balls, Exp Therm Fluid Sci 38 (2012) 134–139. https://doi.org/10.1016/j.expthermflusci.2011.12.002.

[37] M. Bagnasco, L. Bottura, M. Lewandowska, Friction factor correlation for CICC's based on a porous media analogy, Cryogenics (Guildf) 50 (2010) 711–719. https://doi.org/10.1016/j.cryogenics.2010.06.016.

[38] S. Du, Z.-X. Tong, H.-H. Zhang, Y.-L. He, Tomography-based determination of Nusselt number correlation for the porous volumetric solar receiver with different geometrical parameters, Renew Energy 135 (2019) 711–718. https://doi.org/10.1016/j.renene.2018.12.001.

[39] X.F.R. Viskanta, J.P. Gore, Measurement and correlation of volumetric heat transfer coefficients of cellular ceramics, Exp Therm Fluid Sci 17 (1998) 285–293. https://doi.org/10.1016/S0894-1777(98)10002-X.

[40] L.B. Younis, R. Viskanta, Experimental determination of the volumetric heat transfer coefficient between stream of air and ceramic foam, Int J Heat Mass Transf 36 (1993) 1425–1434. https://doi.org/10.1016/S0017-9310(05)80053-5.